EPJ .org
● ● ● ● ●
● ● ● ● ●

RESEARCH ARTICLE

Open Access

General considerations for effective thermal neutron shielding in detector applications

Alexander Backis[1,2*], Ramsey Al Jebali[1,2], Kevin Fissum[2,3], Phillip Bentley[2], Richard Hall-Wilton[1,2,4,5], Kalliopi Kanaki[2], Thomas Kittelmann[2] and Kenneth Livingston[1]

*Correspondence:
a.backis.1@research.gla.ac.uk
[1]School of Physics & Astronomy,
University of Glasgow, Glasgow, UK
[2]European Spallation Source ERIC,
Lund, Sweden
Full list of author information is
available at the end of the article

Abstract

For thermal neutron detectors, effective shielding is a crucial aspect of signal-to-background optimization. This is especially important for cold to thermal neutrons, as the detectors are most sensitive in this energy range. In this work, a few common shielding materials, such as cadmium, B_4C and epoxy-Gd_2O_3 mixtures, are analytically evaluated based on interaction cross sections extracted from Geant4. For these materials, the neutron absorption and scattering dependence on material thickness and incident neutron energy are examined. It is also considered how the absorption and scattering change with different material compositions, such as ^{10}B-content in B_4C, and component ratio in epoxy-Gd_2O_3 mixtures. In addition, a framework is introduced to quantify the effectiveness of the neutron shielding, comparing the relationship between absorption and scattering of different shielding materials. The aim is to provide a general tool kit, which can be used to quickly identify an appropriate shielding material, with the required thickness, to reach a desired thermal neutron shielding performance. Finally, as an example, the developed tool kit is applied to the specific shielding application for the Multi-Grid CSPEC detector, currently in development for the European Spallation Source.

Keywords: Neutron detectors; Neutron shielding; Neutron instruments; Simulation

1 Introduction

Effective neutron shielding is an essential component in signal-to-background ratio optimization for thermal neutron detectors. The purpose of the shielding is to decrease both the flux of *internally scattered neutrons* and *external background neutrons* entering the active detector volume, thereby increasing the signal-to-background ratio. This is important, as the performance gains from decreased background can sometimes exceed those from an increased source brightness [1, 2]. To decrease the background, the general approach is to apply shielding on all internal and external detector surfaces not directly illuminated by the incident neutrons. This shielding is especially important for neutrons with energies that the neutron detector are optimized to detect, which, for detectors in neutron scattering instruments, is commonly cold to epithermal neutrons.

Cold to epithermal neutron shielding for detector applications has been studied previously, see for example [3–5]. In these investigations, the focus was on the boron-10

🦄 Springer

based Multi-Grid detector [6–10], developed for the CSPEC [11, 12] and T-REX [13] spectroscopy instruments at the upcoming European Spallation Source (ESS) [14–17]. The investigations were done using a combination of measurement data and Geant4 [18–20] simulations. The focus was to reduce the background from internally scattered neutrons by applying internal shielding. Another excellent resource on neutron shielding for detector applications can be found in [21], where several shielding materials are examined experimentally.

In this work, however, a more general method for examining the effectiveness of different shielding configurations is presented. The aim is to provide an easy-to-use procedure, based on analytical calculations, to identify potential shielding configuration candidates. By following the procedure, it is possible gain a fair idea of which shielding materials, and with what thicknesses, are necessary to reach a certain signal-to-background ratio (SBR). This is beneficial because it can be time-consuming to implement and run full-scale detector simulations. Furthermore, the search space of possible shielding configurations depends on many parameters, which adds to the complexity of finding a good shielding option. Therefore, it is crucial to have a method to narrow down the possible shielding candidates as much as possible at an early stage.

To quantitatively evaluate and compare different shielding configurations, a SBR metric, with reference to a generic detector geometry, is introduced to measure the amount of background neutrons entering the active detector volume. Each shielding configuration is divided into four components, one for external shielding and three for internal shielding, where each component is assigned a unique way of measuring its contribution to the overall background. This is because, depending on where shielding is situated on the detector, it will serve different purposes, and will therefore require separate ways to measure its performance. For example, the purpose of the external shielding is to keep out outside neutrons, so the only thing which should be considered is how much transmission the shielding has. This is in contrast with internal shielding, where it is also necessary to consider how much of the incident neutrons on the shielding scatter back into the active volume.

Note that the SBR metric gives an overall indication of the effectiveness of the shielding, but, of course, there are several other factors which should be considered before reaching a final decision on shielding material. These might include the level of gamma-emissions from the neutron absorption reactions, as well as the toxicity, activation, machinability and cost and durability of materials, among others. A discussion of many of these practical aspects can be found in [21], where several neutron shielding materials are evaluated. For example, one important consideration mentioned is that gadolinium sheets are around 8 to 13 times more expensive than cadmium sheets, which is a crucial detail to consider when evaluating shielding candidates. It is also considered in what shapes shielding materials are commercially available in and if personnel safety is a concern, among other factors. A detailed investigation of these aspects is, however, beyond the scope of this work.

The SBR metric depends on two attributes of the shielding materials. The first is the amount of neutrons being transmitted through the shielding, *transmission*, and the second is the amount of back-scattered neutrons which re-emerge into the active volume, *albedo*. To analytically calculate the value of these, it is approximated that the dominant factors are the neutron absorption and scattering probabilities in the materials. To find these, the interaction cross sections are first extracted from Geant4 (version 10.4.3) us-

ing the ESS Detector Group (DG) framework [22, 23], where the QGSP_BIC_HP_EMZ Geant4 physics list is used. Using the extracted interaction cross sections, the corresponding interaction probabilities are found using the mean free path approximation, which uses the cross sections together with the average atomic density and material thickness. The derivation of the interaction probability formula is outlined in for example [24].

For most materials studied, the NCrystal thermal neutron transport library is used [25–27]. By creating materials with this library, molecular structures and crystal properties are considered, which allows for effects such as Bragg reflections to be accounted for. This gives a more accurate modeling of how incident thermal neutrons interact with the materials and enhances the precision of the investigation.

To find a suitable shielding configuration, the performance of appropriate shielding material candidates are compared. These materials include, cadmium, Gd_2O_3, LiF, B_4C, epoxy-Gd_2O_3 mixtures, epoxy-B_4C mixtures, MirroBor [28] and Boral [29]. The epoxy used in the investigations is based on the Araldite 506 epoxy resin $C_{54}H_{60}O_9$ [30]. In the investigations, it is also examined how the transmission and albedo can change for real world materials if, for example, the enrichment level of ^{6}Li and ^{10}B is varied, or if the weight ratio between epoxy and Gd_2O_3 is altered.

In the last section of this work, the methodology presented in earlier sections is applied to a specific shielding application, namely the Multi-Grid CSPEC detector, and a suitable shielding configuration is found which fulfills the performance requirement.

2 Metric

To evaluate and compare different shielding configurations, a quantitative performance metric is needed. As the purpose of the shielding is to optimize SBR by reducing background entering the active detector volume, this is a good metric to quantify the effectiveness of a shielding. The SBR in this work, for a specific neutron energy E_n, is defined according to equation (1),

$$\text{SBR}(E_n) = \frac{\phi^{signal} \cdot \epsilon^{detection}}{\phi^{background} \cdot \epsilon^{detection}}\bigg|_{E_n} = \frac{\phi^{signal}}{\phi^{background}}\bigg|_{E_n}, \tag{1}$$

where ϕ^{signal} and $\phi^{background}$ is flux (neutrons/unit time) of signal and background neutrons, respectively, entering the active detector volume, while $\epsilon^{detection}$ is the neutron detection efficiency. Note that, in the last step, it is assumed that the neutron detection efficiency is identical for all neutrons, signal and background, with the same energy entering the active volume. This is not strictly correct, as the neutron incident angle can affect detection efficiency. However, to keep the definition as general as possible, and to facilitate calculations, this is the approximation which is used.

The first step in determining the SBR is to define which background sources are considered. This is presented in Fig. 1, where the top view of a general detector shielding layout is presented together with the background sources studied in this work. The background include stray neutrons entering the active detector volume from anywhere except the entry window (1), albedo neutrons from the vessel walls and back (2), neutrons which are scattered inside the active detector volume (3), and albedo neutrons from the shielding materials themselves (4).

To attenuate these backgrounds, shielding is introduced externally and in all internal pathways where neutrons can scatter, as seen in Fig. 1. The shielding configuration is

Figure 1 Top view of a general neutron detector, displaying the background neutrons together with the shielding configuration designed to attenuate them. In the figure, the vessel (dark grey) and active detector volume (light grey) are presented together with different categories of shielding (interstack, external, end and side shielding). The numbers associated with the arrows highlight the different types of backgrounds and include: (1) external background, (2) scattering in the vessel, (3) scattering in the active volume and (4) scattering of the shielding materials

divided into four generic components, namely external shielding (purple), end shielding (red), side shielding (blue) and interstack shielding (green). To evaluate the effectiveness of the shielding, it is here considered, for each of the shielding components, the probability of an incident neutron upon the shielding to reach the active volume as background. This will be referred to as the probability of the incident neutron to "become background". This is a useful concept, as it is a general quantity which can be used to directly compare the different shielding components. A neutron can end up as background either through transmission, albedo or a combination of the two processes, where the exact details depends on the specific shielding component. To simplify the considerations, neutrons are assumed to always hit the shielding perpendicularly and all scattering interactions are approximated to be elastic.

The purpose of the external shielding is to keep out outside neutrons, so the probability of an incident neutron upon the external shielding to become background, $P_{external}$, is simply the probability of the neutron to be transmitted through the shielding and reaching the active volume ($P_{transmission}$). This is in contrast with the interstack shielding, which serves two purposes: preventing scattered neutrons from reaching the adjacent active volume, while at the same time not scatter them back. Consequently, the probability of an incident neutron upon the interstack shielding to become background, $P_{interstack}$, depends on both the transmission and albedo probabilities ($P_{transmission} + P_{albedo}$).

For the side and end shielding, the probability for an incident neutron to become background, P_{side} and P_{end}, respectively, similarly depends on two terms. The first terms represents the amount of neutrons which are transmitted through the shielding, back-scatters in the vessel, and are transmitted back into the active volume ($P_{transmission} \cdot P_{vessel\,albedo} \cdot$

$P_{transmission}$), while the second term is neutron albedo of the shielding itself (P_{albedo}). To be as general as possible, and to simplify the calculations, a worst case scenario is applied and $P_{vessel\,albedo} = 1/2$. That is, if a neutron reaches the vessel, there is a 50% probability that it will scatter back towards the active volume.

The probabilities, for each shielding component, of an incident neutron with an energy E_n upon the shielding to reach the active volume as background are summarized in equations (2a) to (2d),

$$P_{external}(E_n) = P_{transmission}\Big|_{E_n}, \tag{2a}$$

$$P_{side}(E_n) = P_{transmission}^2 \cdot \frac{1}{2} + P_{albedo}\bigg|_{E_n}, \tag{2b}$$

$$P_{end}(E_n) = P_{transmission}^2 \cdot \frac{1}{2} + P_{albedo}\bigg|_{E_n}, \tag{2c}$$

$$P_{interstack}(E_n) = P_{transmission} + P_{albedo}\big|_{E_n}, \tag{2d}$$

where $P_{transmission}$ is squared for P_{side} and P_{end} because the neutrons have to travel through the shielding twice during their round-trip.

Next, the difference in incident flux upon the separate shielding components is considered. This is to get a clearer understanding of the relative importance of each shielding component, which is generally not equal. The background flux due to the different shielding components is presented in equations (3a) to (3d), which show the relationship between incident neutron flux, $\phi^{incident}$, and the background flux which escapes the shielding, $\phi^{background}$, for neutrons with energy E_n,

$$\phi_{external}^{background}(E_n) = \phi_{external}^{incident} \cdot P_{external}\big|_{E_n}, \tag{3a}$$

$$\phi_{side}^{background}(E_n) = \phi_{side}^{incident} \cdot P_{side}\big|_{E_n}, \tag{3b}$$

$$\phi_{end}^{background}(E_n) = \phi_{end}^{incident} \cdot P_{end}\big|_{E_n}, \tag{3c}$$

$$\phi_{interstack}^{background}(E_n) = \phi_{interstack}^{incident} \cdot P_{interstack}\big|_{E_n}, \tag{3d}$$

where the subscript indicates which background component the flux refers to.

Using equations (3a) to (3d), the SBR defintion in equation (1) can be expanded to,

$$\mathrm{SBR}(E_n) = \frac{\phi^{signal}}{\phi_{external}^{background} + \phi_{side}^{background} + \phi_{end}^{background} + \phi_{interstack}^{background}}\Bigg|_{E_n}. \tag{4}$$

Note that each shielding components is treated independently of the others. That is, in this simplified model, an increased thickness of the side and end shielding does not decrease the amount of external neutrons entering the detector, which would be the case in a real world application. Instead, this amount is completely determined by the thickness of the external shielding. The motivation for this is, again, to keep the model as simple as possible.

3 Calculations
To determine the efficiency of the shielding, it is necessary to evaluate the expressions in equations (2a) to (2d), which contains the "incident neutron on shielding to background"-

probabilities. As all of these probabilities depend upon $P_{transmission}$ and P_{albedo}, it is sufficient to determine these two quantities to evaluate the expression for all four shielding components. However, to do this is analytically and in a general fashion, a few approximations and assumptions are required. Therefore, a simplified model is introduced to perform the calculations.

As a starting point, it is assumed that the transmission and albedo is completely determined by the neutron absorption and scattering probabilities in the material. To calculate these probabilities, the formula for interaction probability, $P_{interaction}$, for a neutron with energy E_n traveling through a material of depth d is used. This is presented in equation (5),

$$P_{interaction}(E_n, d) = 1 - \exp\left[-\Sigma(E_n) \cdot d\right], \tag{5}$$

where Σ is the macroscopic interaction cross section, defined according to equation (6),

$$\Sigma(E_n) = \sigma(E_n) \cdot N, \tag{6}$$

where σ is the microscopic interaction cross section and N is the atomic number density. The atomic number density N $[\text{cm}^{-3}]$ relates to the weight density ρ $[\text{g} \cdot \text{cm}^{-3}]$ according to equation (7),

$$N = \frac{\rho}{A} \cdot N_A \cdot N_{atoms\,per\,molecule}, \tag{7}$$

where A is the molecular weight $[\text{g} \cdot \text{mol}^{-1}]$, N_A is Avogadro's number $[6.022 \cdot 10^{23}\ \text{mol}^{-1}]$, and $N_{atoms\,per\,molecule}$ is the number of atoms per molecule. Note that for molecules and composite materials, σ and N are calculated as atomic averages.

As the values of σ and N are material dependent, it is necessary to introduce a set of potential shielding materials to do explicit calculations. These are presented in Table 1, where a summary of all materials used in this work are seen together with their corresponding average atomic densities $\bar{N}$ and chemical composition. Note that the materials are grouped based on their relative complexity, i.e. pure elements, molecules and compounds of molecules. The values of $\bar{N}$ were extracted using the ESS DG simulation framework.

An ideal shielding material is "black", i.e. it absorbs all neutrons incident upon it, none are transmitted through it, and none are reflected or scattered. Therefore, most of the materials in the table were chosen due to their large content of highly neutron absorbing isotopes, such as ^{6}Li, ^{10}B, ^{113}Cd and ^{157}Gd, which gives the materials good shielding properties. However, a few materials, namely aluminum and epoxy, were chosen for a different reason. These materials do not contain any strong neutron absorbing isotopes, but they might be used internally in detectors. Therefore, it is important to know how much scattering they would introduce. Finally, polyethylene is also investigated due to its large hydrogen content and consequent neutron scattering properties. This makes it a reference for what a "worst case scenario" in terms of scattering might look like.

The materials investigated are implemented in two different ways to study neutron scattering, as highlighted by the asterisks and daggers in the table. Most of the materials are implemented as NCrystal materials, due to the extra information available concerning material structure. There are, however, a few exceptions, and these are implemented as stan-

Table 1 Summary of materials used, showing their molecular composition, weight distribution, enrichment level, and average atomic number densities $\bar{N}$. Materials implemented as standard Geant4 materials are marked with asterisks, while materials implemented using NCrystal are marked with daggers. Note that for personnel safety reasons, the amount of gamma rays produced from the neutron absorption reactions in the materials should be considered

Material	Composition	wt%	Enrichment [at%]	$\bar{N}$ [cm^{-3}]
ELEMENTS				
Cadmium*	Cd	100		$4.63401 \cdot 10^{22}$
Aluminum†	Al	100		$6.02325 \cdot 10^{22}$
MOLECULES				
Gadolinium oxide*	$^{nat}Gd_2O_3$	100		$6.15251 \cdot 10^{22}$
Boron carbide (natural)†	$^{nat}B_4C$	100	^{10}B/B: 20	$1.36702 \cdot 10^{23}$
Boron carbide (enriched)†	B_4C	100	^{10}B/B: 99	$1.36712 \cdot 10^{23}$
Lithium fluoride (natural)†	^{nat}LiF	100	^{6}Li/Li: 8	$1.23396 \cdot 10^{23}$
Lithium fluoride (enriched)†	LiF	100	^{6}Li/Li: 99	$1.23392 \cdot 10^{23}$
Epoxy†	$C_{54}H_{60}O_9$	100		$1.02462 \cdot 10^{23}$
Polyethylene†	C_2H_4	100		$1.18497 \cdot 10^{23}$
COMPOUNDS				
Epoxy – Gadolinium oxide*	$C_{54}H_{60}O_9$	50		$9.68366 \cdot 10^{22}$
(50 – 50)	$^{nat}Gd_2O_3$	50		
Epoxy – Gadolinium oxide*	$C_{54}H_{60}O_9$	35		$9.30040 \cdot 10^{22}$
(35 – 65)	$^{nat}Gd_2O_3$	65		
Epoxy – Boron carbide†	$C_{54}H_{60}O_9$	50		$1.13422 \cdot 10^{23}$
(natural)	$^{nat}B_4C$	50	^{10}B/B: 20	
Epoxy – Boron carbide†	$C_{54}H_{60}O_9$	50		$1.13861 \cdot 10^{23}$
(enriched)	B_4C	50	^{10}B/B: 99	
MirroBor*	$^{nat}B_4C$	80	^{10}B/B: 20	$7.95206 \cdot 10^{22}$
	C	14		
	O	5		
	H	1		
Boral†	Al	90		$6.83984 \cdot 10^{22}$
(90 – 10)	$^{nat}B_4C$	10	^{10}B/B: 20	
Boral†	Al	33		$1.12700 \cdot 10^{23}$
(33 – 67)	$^{nat}B_4C$	67	^{10}B/B: 20	

* Implemented as standard Geant4 material.

† Implemented as NCrystal material.

dard Geant4 materials. The first reason for this is that NCrystal does currently not support materials with resonance frequencies in the cold to thermal energy range, which is why the cadmium, Gd_2O_3 and the Epoxy-Gd_2O_3 mixtures are all implemented as standard Geant4 materials. Note that in the Epoxy-Gd_2O_3 mixtures, both the Epoxy and Gd_2O_3 are implemented as standard Geant4 materials, as mixtures between standard Geant4 and NCrystal materials is currently not possible. The second reason NCrystal is not used, as in the case for MirroBor, is because the molecular structure formula of the material was not known at the time of writing.

For the compound materials in the table, approximations of the total weight densities are used for materials without table values, such as the epoxy-Gd_2O_3 mixtures. This is done by first assuming that the weight density of each of the components does not change when they are part of a compound. After that, the volumetric fraction of each component needed to achieve a specific weight ratio, for example 50 wt% epoxy and 50 wt% B_4C, is calculated. Using the obtained volumetric fractions for each component, the resultant density of the compound is calculated. This calculation, for a mixture of two materials, is

shown in equations (8a) and (8b),

$$\frac{w_1}{w_2} = \frac{x \cdot \rho_1}{(1-x) \cdot \rho_2} \quad \Leftrightarrow \quad x = \frac{w_1 \cdot \rho_2}{w_1 \cdot \rho_2 + w_2 \cdot \rho_1}, \tag{8a}$$

$$\rho_{12} = x \cdot \rho_1 + (1-x) \cdot \rho_2, \tag{8b}$$

where w_1 and w_2 are the weight percentages in the mixture of component 1 and 2, and ρ_1 and ρ_2 are the weight densities of component 1 and 2, respectively. Furthermore, x and $x - 1$ are the volumetric fractions of component 1 and 2, respectively, and ρ_{12} is the weight density of the mixture of component 1 and 2.

The next step is to extract the average microscopic absorption and scattering cross sections, separately, for these shielding materials. For the scattering cross sections, this is the sum of cross sections for all types of scattering, including those for coherent elastic, coherent inelastic, incoherent elastic and incoherent inelastic scattering. This is presented in Fig. 2. Using the microscopic cross sections in Fig. 2 together with the atomic number densities in Table 1, the macroscopic cross sections of the materials can now be calculated. This is presented in Fig. 3.

Using the macroscopic absorption and scattering cross sections together with equation (5), the absorption and scattering probabilities, $P_{absorption}$ and $P_{scattering}$, respectively, are calculated according to equations (9a) and (9b),

$$P_{absorption}(E_n, d) = 1 - \exp\left[-\Sigma_{absorption}(E_n) \cdot d\right], \tag{9a}$$

$$P_{scattering}(E_n, d) = 1 - \exp\left[-\Sigma_{scattering}(E_n) \cdot d\right], \tag{9b}$$

where $\Sigma_{absorption}$ and $\Sigma_{scattering}$ are the macroscopic absorption and scattering cross sections, respectively.

Using the absorption and scattering probabilities, the next step is to estimate the transmission and albedo of the shielding materials. To simplify the calculations, a one-dimensional model representing the three-dimensional scattering problem is used. In the model, only single scattering interactions are considered and all scattering is assumed to be isotropic and elastic. This means that half the neutrons are forward-scattered, and half are back-scattered.

Another consequence of using a one-dimensional model, is that the effect of different incident angles, as well as different scattering angles, are not accounted for. Therefore, the only neutrons considered are those that are incident along the normal of the shielding material, i.e. neutrons incident at a perpendicular angle with respect to the shielding material plane. Neutrons that scatter will be assumed to scatter along that same line, either forward or backward.

For a neutron to be transmitted, it is required that the neutron is not absorbed or back-scattered during its passage through the shielding. This is illustrated in Fig. 4. Therefore, the probability of a neutron being transmitted can be expressed as the joint probability of both these conditions being fulfilled simultaneously.

As the probability of being absorbed is given by $P_{absorbed}$, it follows that the probability of not being absorbed is the inverse of this ($P_{not\,absorbed} = 1 - P_{absorbed}$). Furthermore, as the
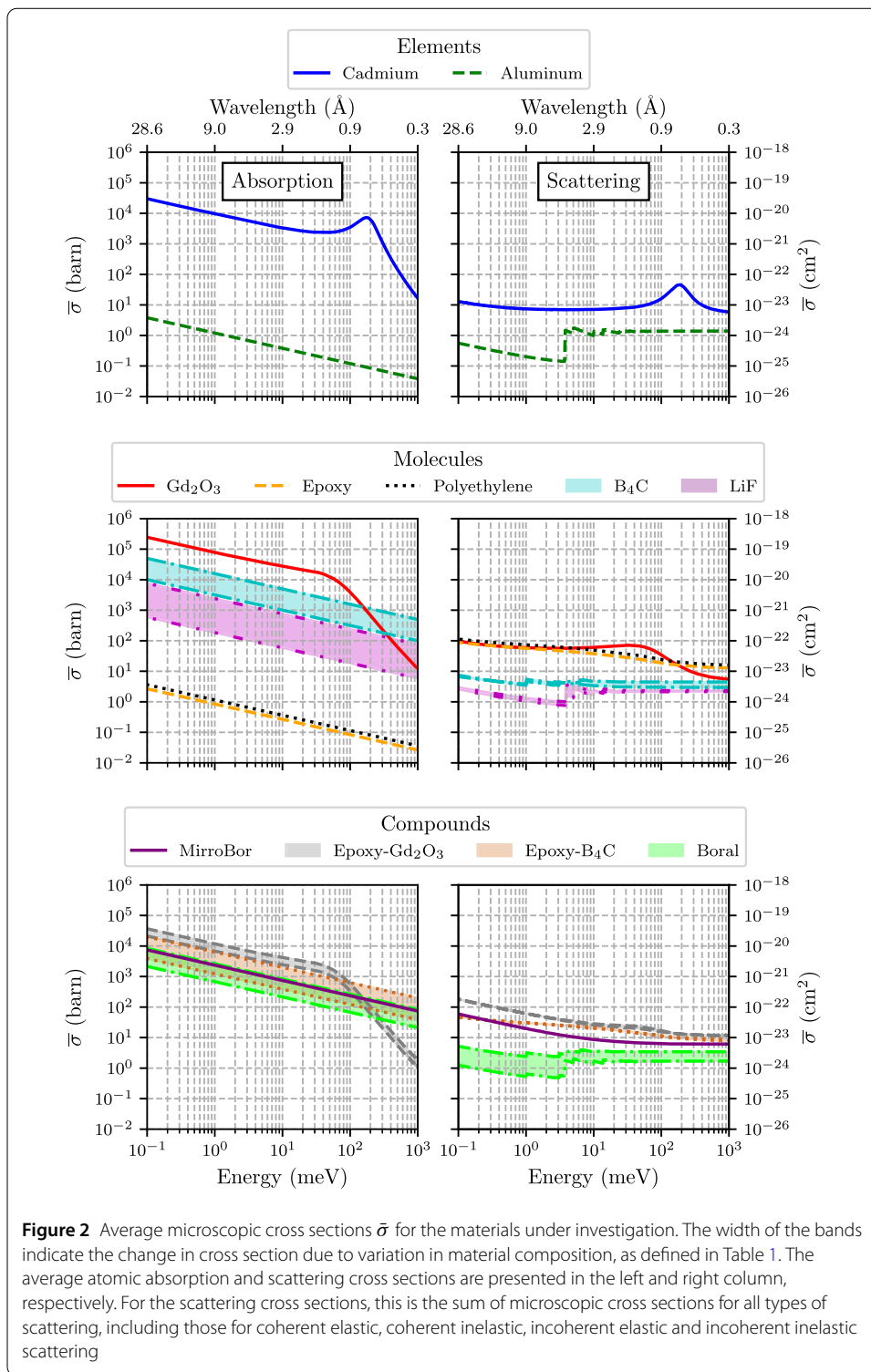
Figure 2 Average microscopic cross sections $\bar{\sigma}$ for the materials under investigation. The width of the bands indicate the change in cross section due to variation in material composition, as defined in Table 1. The average atomic absorption and scattering cross sections are presented in the left and right column, respectively. For the scattering cross sections, this is the sum of microscopic cross sections for all types of scattering, including those for coherent elastic, coherent inelastic, incoherent elastic and incoherent inelastic scattering

scattering is assumed to be isotropic, there is a 50% probability that the neutron is back-scattered if it is scattered, i.e. $P_{back-scattered} = \frac{1}{2}P_{scattered}$. Hence, the probability of not being back-scattered is given by the inverse of this $(1 - \frac{1}{2}P_{scattered})$. Therefore, the transmission probability, $P_{transmission}$, of a neutron with energy E_n incident on a shielding with thickness

Figure 3 Average macroscopic cross sections $\bar{\Sigma}$ for the materials under investigation. The width of the bands indicate the change in cross section due to variation in material composition, as defined in Table 1. The average macroscopic absorption and scattering cross sections are presented in the left and right column, respectively. For the scattering cross sections, this is the sum of macroscopic cross sections for all types of scattering, including those for coherent elastic, coherent inelastic, incoherent elastic and incoherent inelastic scattering

d is given by equation (10),

$$P_{transmission}(E_n, d) = (1 - P_{absorption}) \cdot \left(1 - \frac{1}{2} P_{scattering} \right) \Bigg|_{E_n, d}. \tag{10}$$

Figure 4 Visualization of the one-dimensional transmission calculation for neutrons incident on a shielding with thickness d. For a neutron to be transmitted, it is required that the neutron is not absorbed or back-scattered in the shielding

Figure 5 Visualization of the one-dimensional albedo calculation for neutrons incident on a shielding with thickness d, illustrating how the shielding is divided into N segments. In the figure, the albedo contribution from the i:th segment is shown, which is highlighted in red. The segment thicknesses are assigned equal lengths on a one-dimensional logarithmic coordinate system. This is to facilitate calculations, which are needed over several orders of magnitude. Note that the neutrons are assumed to scatter from the deepest end of the segment

For an incident neutron to become albedo, it is required that neutron is back-scattered at some point in the shielding, that the neutron is not absorbed on the way to that point, and that it is not absorbed on the way back out from that point. This is visualized in Fig. 5. As the joint probability of these three conditions being fulfilled simultaneously is strongly dependent on where along the depth of the shielding the neutron is scattered, the shielding depth d is split into N segments which are considered individually. The total albedo probability is then calculated as the sum of the albedo contributions from all the segments. In the figure, the albedo contribution from the i:th segment is shown.

To calculate the total albedo probability, the first step is to calculate the probability for a neutron to become albedo from an arbitrary segment i. For a neutron to become albedo in segment i, it must not be absorbed on the path leading up to the segment, nor in the segment itself. This probability is given by $(1 - P^i_{absorption})$, where the superscript indicates the thickness, as seen in Fig. 5. Furthermore, it has to be back-scattered in the segment, which has a probability given by $\frac{1}{2}(P^i_{scattering} - P^{i-1}_{scattering})$. Note that the probabilities are subtracted because they are accumulated probabilities, while the factor $\frac{1}{2}$ is due to the assumption of isotropic scattering. Finally, the neutron must not be absorbed on the way back, as it passes the same amount of shielding a second time. This probability is equal to the probability of not being absorbed on the way in $(1 - P^i_{absorption})$, as it is the same path length.

Figure 6 Transmission and albedo probability at a fixed energy, 25.25 meV (1.80 Å), as a function of thickness for the materials under investigation. The width of the bands indicate the change in probability due to variation in material composition, as defined in Table 1. The transmission is presented to the left and the albedo to the right
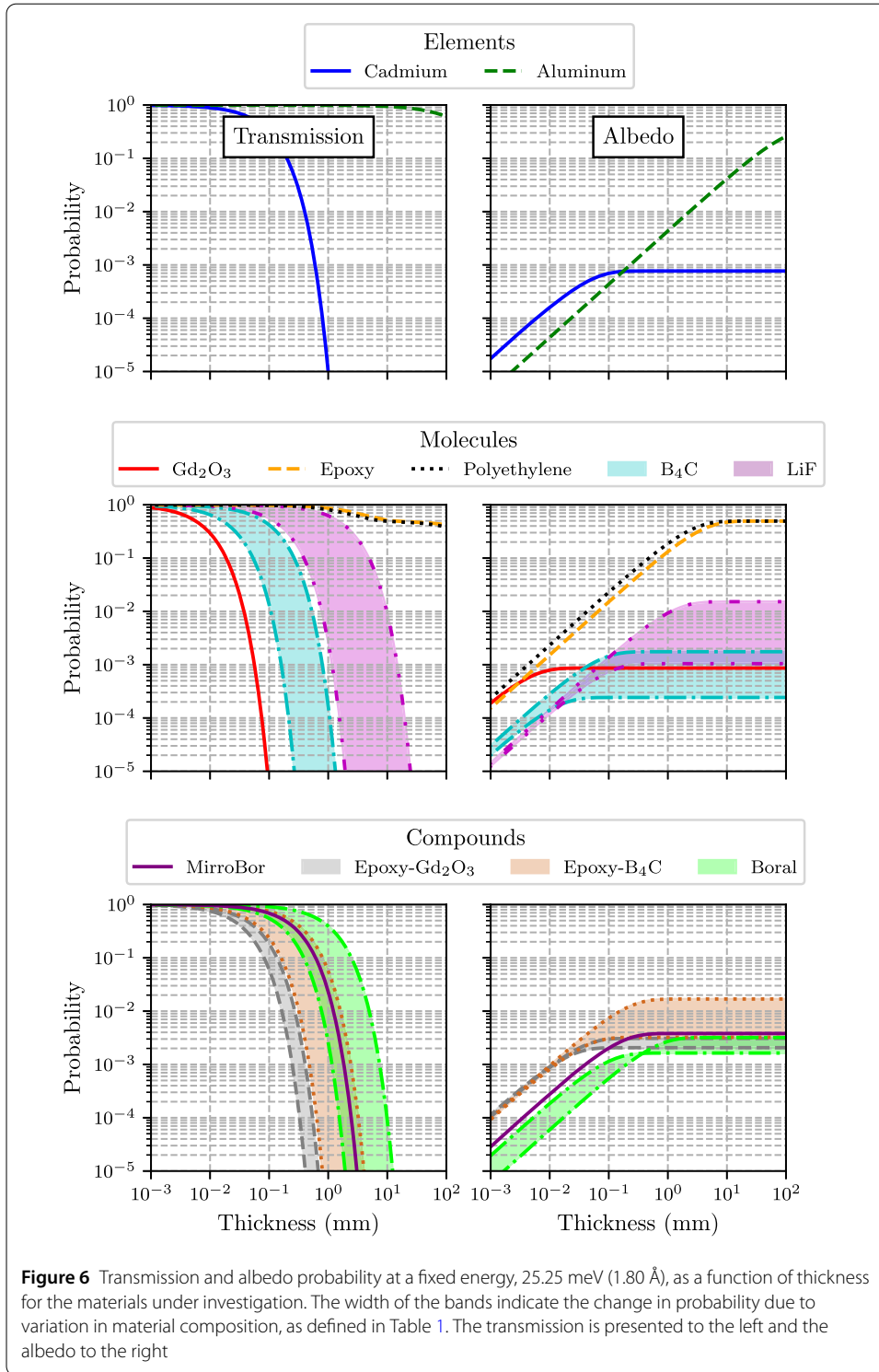
Putting this together, gives the probability of albedo from a segment i, P^i_{albedo}, according to equation (11),

$$P^i_{albedo}(E_n) = \left(1 - P^i_{absorption}\right)^2 \cdot \frac{1}{2}\left(P^i_{scattering} - P^{i-1}_{scattering}\right)\bigg|_{E_n}, \tag{11}$$

where $(1 - P^i_{absorption})$ is squared because it appears twice. From this expression, the total albedo probability, P_{albedo}, can be calculated according to equation (12),

$$P_{albedo}(E_n, d) = \sum_{i=1}^{N} \left(1 - P^i_{absorption}\right)^2 \cdot \frac{1}{2}\left(P^i_{scattering} - P^{i-1}_{scattering}\right)\Bigg|_{E_n}, \tag{12}$$

where the summation is over all segments in the shielding layer.

Using the above approximations, the neutron transmission and albedo probabilities are calculated as a function of thickness for the shielding materials under consideration. This is presented in Fig. 6, where an example is presented at 25.25 meV (1.80 Å). As can be seen, the transmission level *decreases* with increased material thickness, while the albedo level exhibits an almost opposite trend: it *increases* with shielding thickness, up until a saturation level is reached.

4 Validity

To investigate the accuracy of the calculations and the simplifications assumed, a series of simulations are performed. The aim of the simulations is to investigate the transmission and albedo probabilities when a more realistic scattering and physics model is used, and compare the results with the calculations. The simulation setup was implemented using the ESS DG simulation framework and was designed to be as general as possible, with the aim to only probe two properties of the shielding materials: how many of the incident neutrons are transmitted and how many become albedo. The setup and geometry used for the simulations are shown in Fig. 7.

The simulation consists of three volumes and a particle generator. The volumes include a thin cylinder target and two semi-spheres, one for transmission and one for albedo, which together fully encapsulates both the particle generator and the target. The particle generator fires a pencil beam of monochromatic neutrons at a perpendicular angle towards the center of the target, whereafter the neutrons are either transmitted and detected in the

Figure 7 Geometry used for simulations, showing the shielding material (green "coin"), incident neutrons (red line), transmission detector (orange half sphere), and albedo detector (blue half sphere). In the left figure, the albedo detector is transparent to show the incident neutrons and shielding material, while in the right figure, both the albedo and transmission detectors are seen fully encapsulating the shielding material and incident neutrons

Figure 8 Cadmium, a one-dimensional comparison between calculation and simulation, where the transmission and albedo comparisons are shown in the left and right plot, respectively. The comparison is done for three different energies, 0.10 meV (28.60 Å), 25.25 meV (1.80 Å) and 1000.00 meV (0.29 Å). Calculations are shown as lines while the simulation results are shown as markers, where each marker corresponds to a separate simulation. Error bars show statistical uncertainties, but are too small to be discernible

transmission semi-sphere, become albedo neutrons and are detected in the albedo semi-sphere, or are absorbed in the target.

The parameters which were varied include the energy of the incident neutrons, the thickness of the target, and the material of the target. A parameter scan was performed over all shielding materials, with 20 different energies, logarithmically distributed between 0.1 meV and 1000 meV, and 20 different thicknesses, logarithmically distributed between 10^{-3} mm and 10^2 mm. For each simulation job, 1e6 incident neutrons were used. The results from a representative material, cadmium, is presented in Figs. 8 and 9, where the calculations are compared to the simulation results.

In Fig. 8, the transmission and albedo is presented as a function of thickness for three distinct energies, which is represented by the three different colors. The calculations are presented as lines while the simulations are presented as markers. In Fig. 9, each data point corresponds to a comparison between calculation and simulation for a specific incident neutron energy (x-axis) and shielding thickness (y-axis). The colors correspond to the ratio between calculation and simulation at each data point, calculated via the Log_{10} difference between the calculation and simulation. For example, a green color corresponds to a ratio between the calculations and simulations which is between 1/2 and 2. This represents a close match in value between simulation and calculation. Note that the limits are set between a factor 1/5 and 5 and that values outside this range are projected on the maximum and minimum colors. Additionally, in order to retain adequate statistics, simulation values with a probability below 1e−5 are not included in the analysis. The calculated iso-line for 1e−5 transmission is shown as a black line, which is seen to closely follow where the simulation data drops below 1e−5.

From the results, which is shown for all materials in Figs. 15 to 30 in the Appendix, it is seen that for most materials the simulations and calculations are in excellent agreement,

Figure 9 Cadmium, two-dimensional comparison between calculation and simulation, where the transmission and albedo comparisons are shown in the left and right plot, respectively. The comparison is done for all combinations of 20 energies and 20 thicknesses evenly spread across the energy and thickness region under investigation. The color shows the ratio between calculation and simulation. In order to only display data with a low statistical uncertainty, simulation values below 1e−5 are not included in the analysis. The calculated iso-line for 1e−5 transmission is presented in the left plot as a black line, which is seen to closely follow where the simulation data drops below 1e−5

within a factor 2, over most energies and thicknesses. The divergence is largest for large thicknesses and high energies, where it for some materials exceeds a factor of 3. There is also a strong transmission divergence for some materials, such as the epoxy-Gd_2O_3 mixtures, for low energies when the transmission level drops below 1e−5. For these materials at this transmission level, the calculations underestimate the transmission level by more than a factor 5. Nevertheless, as the calculations and simulations agree within a factor 2 for a majority of the materials for most thicknesses and energies, the calculations are therefore sufficiently accurate to be used to evaluate the degree of shielding need for a detector.

Note that this investigation only probes how well the calculations compare to a more sophisticated simulation method, not real measurement data. However, by studying the measurement data in [21], a brief sanity check is possible for two materials included in this work, namely cadmium (0.4 mm) and aluminum (6.35 mm). For 1.80 Å incident neutrons, these materials have a transmission calculation that agrees well with the measurement results. To perform a measurement comparison for the remaining materials in this work, further studies are needed which are outside the scope of this work.

5 Procedure

Using the analytic approximations for neutron transmission and albedo, which compares well to simulations, it is now possible to quantify the performance of different shielding configurations according to the SBR metric presented earlier. However, to identify the most suitable shielding configuration for a specific application, a procedure to actually pinpoint the most appropriate configuration is needed. The purpose of this section is to present a brief step-by-step guide for finding that configuration.

The first step, is to identify the constraints and requirements of the desired shielding. This includes information about how much space is available for the various shielding components and what the desired SBR is. Next, information is needed about which inci-

dent neutron energy the SBR should be fulfilled at. Finally, it is necessary to approximate how high the incident neutron flux is on the different shielding components. This is to understand the relative importance of shielding the different regions, as the amount of flux they are exposed to is generally not equal.

To simplify the considerations, and to make the discussion as general as possible, the signal and background fluxes are normalized to the signal flux. That is, the signal flux is set to 1, $\phi^{signal} = 1$, and the background fluxes are expressed in relation to the incident flux. This makes the SBR easy to grasp and can be deduced simply by looking at the background levels. Studying equation (4), it is seen that there are several ways of achieving a certain SBR, depending on the relative strength of the background levels from the various shielding components. Nevertheless, it is a requirement that the background from each of the components is below $\frac{1}{SBR}$ to fulfill the SBR demand, and this is the criterion used here to ensure that the SBR requirement is fulfilled.

To find a suitable material, the desired SBR and background flux on the various shielding components are related to the more general quantity of "incident-neutron-to-background"-probability discussed earlier, which is material dependent. This gives the maximal acceptable probability, for each shielding components, to fulfill the SBR criterion. The conversions expressions are presented in equations (13a) to (13d),

$$P_{external} = P_{transmission} = \frac{1}{\phi^{incident}_{external}} \cdot \frac{1}{SBR}, \tag{13a}$$

$$P_{side} = P^2_{transmission} \cdot \frac{1}{2} + P_{albedo} = \frac{1}{\phi^{incident}_{side}} \cdot \frac{1}{SBR}, \tag{13b}$$

$$P_{end} = P^2_{transmission} \cdot \frac{1}{2} + P_{albedo} = \frac{1}{\phi^{incident}_{end}} \cdot \frac{1}{SBR}, \tag{13c}$$

$$P_{interstack} = P_{transmission} + P_{albedo} = \frac{1}{\phi^{incident}_{interstack}} \cdot \frac{1}{SBR}. \tag{13d}$$

Using these equations, the search for suitable shielding materials can start. A good way to start this search, is to determine if the transmission or albedo probability is the limiting factor on performance. Upon closer inspection, as shown in Fig. 10, it is found that at the thickness where the albedo level saturates the transmission level is larger or equal to the albedo level. This is true for all energies and materials under investigation here, signifying that the upper performance limit of a shielding material is given by the albedo saturation level.

This is an important result, as it simplifies the task of selecting the thickness which gives the best trade-off between transmission and albedo. This is because the only information necessary concerning the albedo probability is the saturation level, which determines the maximum performance level. Once this is known, the performance can be completely determined by adjusting the transmission level, which can be tuned to the desired level (limited, of course, by the albedo saturation level) by adjusting the shielding thickness. Note that the albedo saturation thickness is here defined as the thickness where the albedo probability has reached 95% of its maximum. This is due to the very slow increase in albedo as a function of thickness when the albedo probability is close to the saturation level.

By using equations (13a) to (13d) to calculate the required probabilities, Figs. 31 to 43 in the Appendix can be used to identify a shielding material which fulfills these demands.
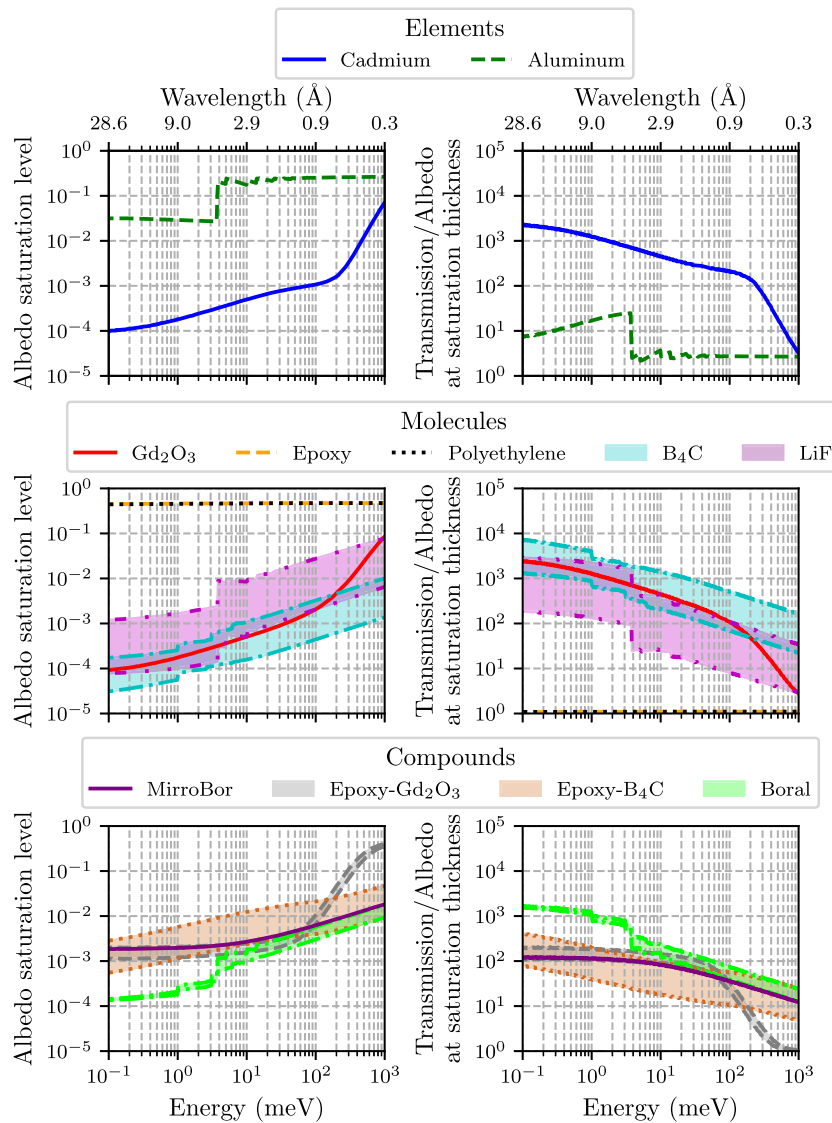
Figure 10 Figure showing the albedo saturation level and a comparison with the transmission level at the saturation thickness. In the left plots, the albedo saturation level is seen, while in the right plots, the ratio between transmission and albedo at the albedo saturation thickness is shown. The width of the bands corresponds to the change in absorption and scattering cross sections due to variation in material composition, as defined in Table 1

Here, cadmium is used as an example, as seen in Fig. 11. In the figure, the probability iso-lines for $P_{transmission}$ (blue) and $P_{transmission}^2 \cdot \frac{1}{2}$ (red) are shown as a function thickness and energy for three different probabilities: 1e−2, 1e−3 and 1e−4. Additionally, the albedo saturation thicknesses are shown as a function of energy, together with the corresponding albedo saturation level for each energy. Note that the albedo saturation level is color coded according to the color bar. By only looking at the energy of interest and up to the maximum thickness allowed for the shielding material, a suitable material can be identified with the thickness that achieves the desired performance. The plots for all shielding materials under investigation is included in the Appendix.

Figure 11 Cadmium, material properterties needed for shielding investigation. The probability iso-lines for $P_{transmission}$ (blue) and $P_{transmission}^2 \cdot \frac{1}{2}$ (red) are shown as a function thickness and energy for three different probabilities: 1e–2, 1e–3 and 1e–4. Additionally, the albedo saturation thicknesses are shown as a function of energy, where the color indicates the albedo saturation level

A step-by-step procedure for finding a shielding material is outlined in Fig. 12, where a flowchart is presented. The flowchart summarizes all the steps discussed above on how to find a shielding configuration to achieve a desired performance at a certain energy.

As a short digression, it is worth mentioning that it is possible to ensemble laminate neutron shieldings by combining two or more different shielding materials in a sequence. This can be especially valuable when the purpose of the shielding is to simultaneously minimize the albedo neutrons and external background neutrons reaching the active detector volume. To do this, the shielding can be split into two components, including an inner shielding (closest to the active detector volume) and an outer shielding (furthest away from the active detector volume). The purpose of the outer shielding is to prevent external neutrons from entering, and can hence have a large scattering contribution. This implies that hydrogenous shielding materials, such as epoxy-B_4C and epoxy-Gd_2O_3, works fine as outer shielding. For the inner shielding, however, a material with less scattering, such as cadmium or B_4C, is required. This is because the purpose of this component is to minimize albedo neutrons.

When designing such a laminate shielding, it is important to know how thick the inner shielding should be to prevent neutrons from reaching the outer shielding, become albedo, and reach the active detector volume in any meaningful quantities. To evaluate this, Figs. 31 to 43 in the Appendix can be consulted. In these figures, the albedo saturation thickness is shown as a function of energy. This saturation thickness is an important

Start

Identify how much space is available for shielding.

Identify the incident neutron energy the shielding should be optimized for.

Identify the SBR requirement.

Approximate the flux on each shielding component, relative to the signal flux.

Use equations (13a) – (13d) to calculate the necessary "incident-neutron-to-background" probabilities for each shielding component to fulfill the SBR requirement.

Go to the figures 31 – 43.

Which shielding component?

External — End, Side or Interstack

Study the blue lines.

Identify the energy of interest on the x-axis. At that energy, search for a material which has an $P_{transmission}$ level which satisfies the requirement for a thickness within the allowed space.

Study the albedo saturation level color curve.

Identify the energy of interest on the x-axis. At that energy, search for a material which has a P_{albedo} saturation level which satisfies the requirement.

At the chosen material, study the blue lines ($P_{transmission}$) if interstack shielding, otherwise look at the red lines ($P_{transmission}^2$).

Identify the energy of interest on the x-axis and the line corresponding to the required probability. Identify the necessary thickness to fulfill the required probability at the energy of interest.

If the thickness is within the allowed space, a suitable shielding material has been found. If not, go back three steps and try to find another material with an acceptable P_{albedo} saturation level.

Finish

Figure 12 Flowchart outlining the procedure to select a suitable shielding material with an appropriate thickness for each shielding component

quantity, as it indicates the largest shielding depth where a neutron has a non-negligible chance of reaching, scatter, and subsequently re-emerge back out of the shielding material as an albedo neutron. Consequently, the saturation thickness can be used as an upper

limit for how thick the inner shielding should be. This is because, any scattered neutron, either in the inner shielding or the outer shielding, has a negligible probability of reaching the active volume beyond the saturation thickness. Hence, the albedo contribution of the outer shielding can be safely discarded with an inner shielding with a thickness equal to the albedo saturation thickness.

If this principle is applied for 1.8 Å (25.25 meV) neutrons, it is seen that, for example, an inner shielding of $\sim$0.2 mm cadmium (corresponding to the albedo saturation thickness in Fig. 31) followed by an outer hydrogenous shielding, such as epoxy-Gd_2O_3 could be combined to create a laminate shielding. It is of course possible to make more detailed investigations concerning shielding laminates with more than two layers, as well as on how much albedo from the outer shielding can be accepted, but this is outside the scope of this work. Furthermore, in the interest of keeping the following discussion simple, only single layer shieldings, i.e. no laminate shieldings, will be considered in the remainder of this work.

Note that this method of designing laminate shieldings is only applicable for the energy regime discussed in this work, i.e. cold to thermal neutron energies. For higher energies, such as MeV neutrons, additional factors has to be considered. This includes, for example, neutron thermalization in the hydrogenated material, which could potentially reduce the incident neutron energies to an energy regime where the detectors are more sensitive. This has to be carefully considered, as it might increase the background level observed. To account for these effects a more advanced study is required, ideally with simulations and measurements, which is outside the scope of this work.

6 Application example: the multi-grid detector for the CSPEC instrument at ESS

The Multi-Grid detector is a large area cold to epithermal neutron detector, developed for time-of-flight neutron spectroscopy. The Multi-Grid detector was invented at the Institut Laue–Langevin (ILL), and has since then been jointly developed with ESS. For neutron detection, the detector employs a Multi-Wire Proportional Counter (MWPC) using 1 bar Ar-CO_2 gas (80:20 volume ratio), coupled with multiple stacks of $^{10}B_4C$-coated aluminum substrates. The coated substrates are called *blades*, and each stack of blades, connected together via perpendicular support blades, is called a *grid*. The grids are kept at ground, and the wires at $\sim$1.1 kV. Neutrons are captured in the coating, and the ejected capture products are detected in the MWPC. Neutron events can then be inferred from coincident signals in the wires and grids, allowing for a 3D-position reconstruction. By stacking several grids into a column, and joining several columns of grids side by side, a large area can be covered. In Fig. 13, an overview of the Multi-Grid CSPEC detector can be seen.

There are a number of free parameters in this design which can be tuned. For example, the coating thicknesses on the blades, the number of blades in each grid, and the dimensions of the grids, can vary from application to application. For the CSPEC detector, the parameters have been designed for cold neutrons, and in Table 2 the most relevant conditions and parameters are presented.

The detector will be utilized in the CSPEC instrument at the upcoming ESS. To attenuate the significant neutron background generated from the source, a numerical approach to optimise the instrument shielding at higher energies has been applied for laminates shieldings, see for example [31]. As the neutron energy increases, however, the neutron

Figure 13 Overview of the Multi-Grid CSPEC detector. In (**a**), a grid is shown, where an example of a blade (red) is highlighted. In (**b**), two columns of grids are seen. Between the cells of the grids, wires will be drawn: one wire per column of aligned cells. In (**c**), the detector vessel is seen, where the two columns of grids will be inserted. Blue arrows represent incident neutrons
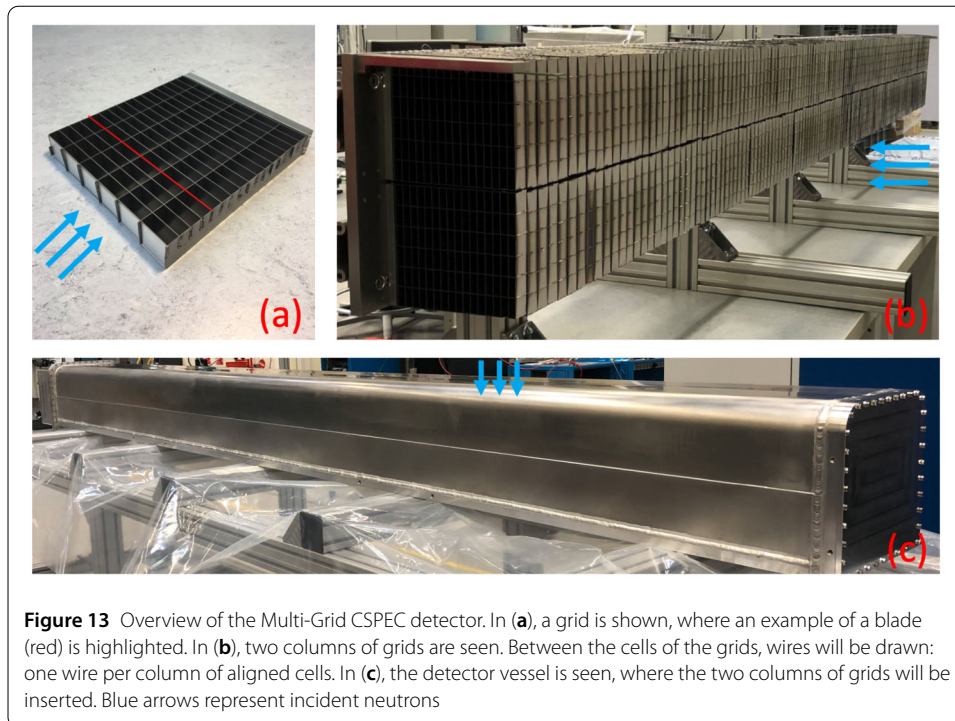
Table 2 Summary of relevant parameters for the Multi-Grid CSPEC detector

Energy to be optimized at	3 meV (5 Å)
Required SBR	10^4
Total normal blade coating thickness	26 μm
Total normal blade substrate thickness	8.5 mm

mean free path in solid materials increases, from length scales of $\lesssim$ mm at thermal energies to tens to hundreds of cm [32] at higher energies, depending on the material density. In air, the mean free path increases from a few m to several hundreds of m [33]. With such long mean free paths, the neutron tracks significantly overlap with multiple component footprints and the component response functions therefore become correlated across the whole facility. The details around the detectors become less important than the transparency of shielding structures, and the albedo of the entire instrument cave and the beam stop. Furthermore, the absorption cross sections are negligible; only scattering is important until the fast neutrons can be moderated down below MeV energies. Other related work has sought to address some of these wider issues [34–36]. Ultimately, for fast neutrons one has to design instrument assemblies more holistically. Such a broad and complex topic is currently being written up as a separate article [37] and so we restrict the scope in the current work to deal with cold and thermal neutrons.

To determine a suitable detector shielding configuration, the flowchart in Fig. 12 is examined. The chart is split into two sections, each focusing on a different aspect. The first part concerns gathering essential information, which includes the maximum thickness allowed for the shielding materials, the required SBR, the incident neutron energy the shielding should be optimized at, as well as approximations of the incident flux on the various shielding components. The second part instructs how to use this information to find shielding materials, with suitable thicknesses, for each of the shielding locations.

Figure 14 Drawing depicting the top view of a CSPEC detector vessel, showing two grid columns placed side-by-side. The available clearances for the interstack shielding (green), end shielding (red) and side shielding (blue) are magnified and marked in units of millimeter
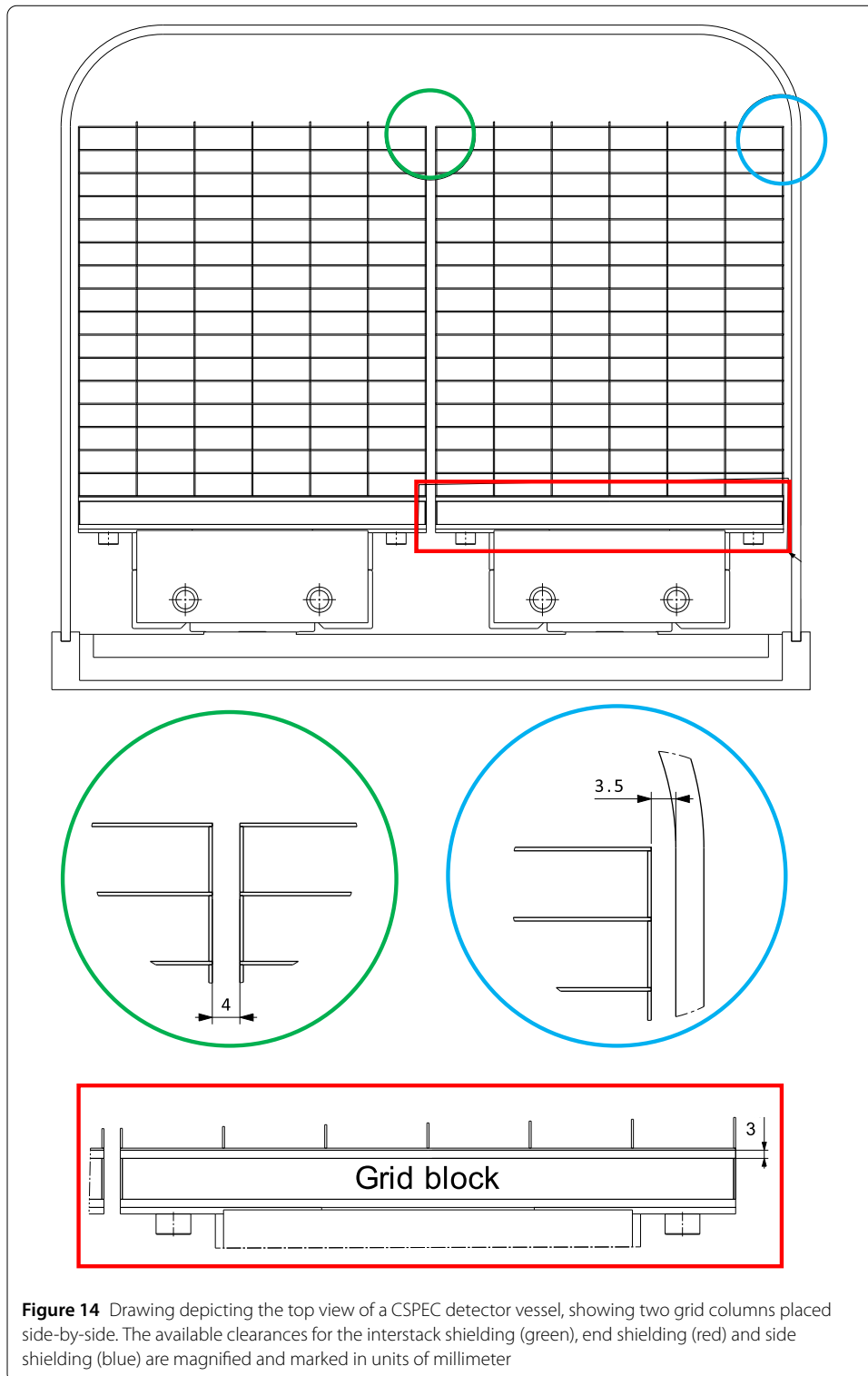
To determine the allowed shielding thicknesses for the different shielding components, Fig. 14 is studied. In the figure, a drawing is presented of the top view of a CSPEC detector vessel. In the drawing, the available space for shielding has been highlighted and magnified, showing the column to column clearance (green), column to inner vessel wall clearance

(blue) and the last blade to grid block clearance (red). These clearances gives 3 mm for the end shielding, 4 mm for the interstack shielding and 3.5 mm each for the side shieldings.

The next step is to approximate the incident neutron flux on the various shielding components. Unfortunately, getting these quantities right can be a complicated task. This is because, for the external shielding, it requires an understanding of the stray neutron background and how it compares to the flux incident on the active detector area. For the end and interstack shielding, in contrast, an intricate knowledge is needed of the behavior of internally scattered neutrons. Therefore, to facilitate the calculations, worst case scenarios will be studied in most cases. To approximate the incident flux on the various shielding components, the values in Table 2 is used.

For the end shielding, $\phi_{end}^{incident}$ can be approximated as the neutron transmission through all the coatings. This is calculated as the transmission probability corresponding to the perpendicular travel path through the B_4C on all the blades (26 μm), which gives a transmission of approximately 5%. That is, $\phi_{end}^{incident} = 5 \cdot 10^{-2}$

For the interstack and side shieldings, $\phi_{interstack}^{incident}$ and $\phi_{side}^{incident}$ can be approximated as the neutron scattering in the aluminum substrates. For the total travel path through 8.5 mm aluminum, this corresponds to a total scattering probability of approximately 5%. Of course, not all of the scattered neutrons will reach the shielding, but it can be used as a high estimate. If it is further assumed that the scattered neutrons are evenly split between the interstack and side shieldings, each shielding will then receive approximately 2.5% each. That is, $\phi_{interstack}^{incident} = \phi_{side}^{incident} = 2.5 \cdot 10^{-2}$.

For the external shielding, the approximation of $\phi_{external}^{incident}$ cannot be directly made. This is because the flux on the external shielding is highly dependent on the background environment inside the instrument, which is not known at the time of writing. However, it is known that the CSPEC detector vessels will be placed in a circumference around the sample position, which means that only the active surface area of the detectors will be in direct line of sight of the incident neutrons. Neutrons reaching the remaining parts of the detectors will either be due to scattering inside the detector tank or external background sources, such as cosmic rays. However, as the exact distribution is not known, a worst case scenario is considered, i.e. the rate on the external shielding is assumed to be equal to that reaching the active detector surface area. That is, $\phi_{external}^{incident} = 1$.

Using the approximated incident fluxes upon the different shielding components together with the required SBR, it is now possible to calculate the required probabilities on the shielding material using equations (13a) to (13d). The results from these calculations, together with the rest of the relevant information collected, are summarized in Table 3. Using the values in the table, it is now possible to select suitable shielding materials.

The external shielding is the most straightforward shielding to find, as the performance only depends on transmission, i.e. $P_{external} = P_{transmission}$. Therefore, only the transmission graphs in the Appendix have to be considered. As there is no information available on how much space is available for the shielding, any material can be selected, as long as the

Table 3 Summary of relevant quantities for selecting a suitable shielding material

	External	End	Side	Interstack
Energy	3 meV (5 Å)			
Available space	N.A.	3.0 mm	3.5 mm	4.0 mm
Required P	1e–4	2e–3	4e–3	4e–3

Table 4 Summary of shielding configuration found for the Multi-Grid detector for the CSPEC instrument to achieve SBR = 1e−4 at 3 meV (5 Å)

	External	End	Side	Interstack
Material	Cadmium	Cadmium	Cadmium	Cadmium
Thickness	0.4 mm	0.1 mm	0.1 mm	0.3 mm

thickness of the material is sufficient to reach a $P_{transmission}$ = 1e−4 transmission level at 3 meV. Studying the blue lines (corresponding to $P_{transmission}$), it is seen that, for example, 0.4 mm of cadmium would fulfill the requirement.

Next, the end shielding is studied. This shielding has a probability dependent on both $P_{transmission}$ and P_{albedo}, according to $P_{end} = P_{albedo} + P_{transmission}^2 \cdot \frac{1}{2}$. As the albedo level is the limiting factor for performance, the first step is to browse through the albedo plots in the Appendix and see if there are any materials which can fulfill the required P_{albedo} = 2e−3 at 3 meV. After scanning the materials, it is concluded that, for example, cadmium fulfills this requirement. The only thing left now is to determine the required thickness to fulfill $P_{transmission}^2 \cdot \frac{1}{2}$ = 2e−3. This is done by looking at the red curves in the transmission plots. As there is no iso-line curve for 2e−3, the closest line is studied, i.e. 1e−3. By studying this curve at 3 meV, it is seen that 0.1 mm of cadmium will fulfill the requirement. As this is well within the allowed space of 3.0 mm, a cadmium shielding of 0.1 mm is adequate.

The side shielding has the same probability as the end shielding, i.e. $P_{side} = P_{albedo} + P_{transmission}^2 \cdot \frac{1}{2}$. There is, however, a difference in the required P between the two shieldings, due to a difference in incident flux. Nevertheless, as the probabilities are only stated in full orders of magnitudes in the plots, the calculations done for the end shielding will be identical for side shielding. Hence, 0.1 mm of cadmium will fulfill the requirement for the side shielding, which is within the available space for shielding at the sides.

The final study concerns the interstack shielding, where the performance is calculated according to $P_{internal} = P_{transmission} + P_{albedo}$. As we know from the above investigation that cadmium can fulfill P_{albedo} = 2e−3 at 3 meV, cadmium is once again chosen. Inspecting the blue curve corresponding to $P_{transmission}$ = 1e−3 in the transmission plot, it is seen that 0.3 mm of cadmium will fulfill the requirement. This is within the available space, and is thus accepted.

At this point, all of the shielding components in the detector have been assigned the required thickness to achieve SBR = 1e−4 at 3 meV. The full shielding configuration is presented in Table 4.

7 Results and discussion

By using a simple one-dimensional model of neutron transmission and albedo, which only considers absorption and scattering probabilities, an easy to use calculation tool was devised to examine different shielding materials. The validity of the calculations was then compared to a general Monte Carlo particle simulation in Geant4, which considers both the real three-dimensional scattering paths in the materials, as well as more complicated physics, such as energy moderation through multiple scatterings. Comparing the results, it was seen that the one-dimensional model gives representative results on transmission and albedo probabilities, as both the simulations and calculations agree within a factor 2 for most materials and energies.

Based on the two properties determined by the calculations, transmission and albedo, the SBR for different shielding configurations could be calculated. Using the SBR as a metric, a quantitative comparison between different shielding options was possible. Each shielding option was split into four different components, including external, end, side and interstack shielding. For each shielding component, the probability of an incident neutron upon it to "become background" was calculated. This is a general quantity which can be used as a common unit to compare all shielding components simultaneously and examine how they contribute to the overall background level.

Using the metric based on SBR, a brief step-by-step guide was developed to find an adequate shielding configuration for a specific requirement. The procedure is based on the observation that the albedo probability, at the saturation level, is always smaller or equal to the transmission probability for all materials under consideration here. This simplifies the task of finding the thickness which gives the best trade-off between transmission and albedo, as the only information necessary is the albedo saturation level, which determines the upper performance. Once this is known, the performance can be completely determined by adjusting the transmission level, which can be tuned to the desired level by adjusting the shielding thickness.

Using the performance metric and procedure outlined in this work, it was possible to find a suitable shielding configuration candidate for the Multi-Grid CSPEC detector. There are of course additional parameters to consider then those discussed here, such as toxicity and machinability of the materials, as well as other engineering factors. However, the above analysis gives a fair idea of what materials are appropriate from a physics point of view, which is a crucial part of the shielding selection process.

8 Conclusions

To improve the signal-to-background ratio in neutron detectors, an appropriate thermal neutron shielding configuration is of key importance. Such a shielding can be found, for example, by using full-scale detector simulations with different shielding configurations and evaluating their different performances. However, such simulations can be time-consuming to implement, and sometimes it is beneficial to use analytical calculations instead. In this work, an easy-to-use analytical procedure for finding an appropriate shielding configuration was presented. The procedure showed that by using a set of simplified calculations for neutron transmission and albedo, together with a set of performance metrics for the shielding materials, it is possible gain a fair idea of which shielding materials, and with what thicknesses, are necessary to reach a certain signal-to-background ratio. Ideally, this final shielding configuration found should then be verified with a full detector simulation, and, if possible, also with measurement data. Nevertheless, using the analytical tools it is possible to explore a vast parameter space of possible shielding configurations, which would be infeasible with full simulations, and identify shielding candidates. This greatly facilitates and accelerates the effort of finding a suitable shielding design.

Appendix

Figures 15 to 30 shows the 2D comparison between calculation and simulation, as described in the main text. In the figures, each data point corresponds to a comparison between calculation and simulation for a specific incident neutron energy (*x*-axis) and

Figure 15 Cadmium, a two-dimensional comparison between calculation and simulation. The transmission and albedo comparisons are shown in the left and right plot, respectively. The comparison is done for all combinations of 20 energies and 20 thicknesses evenly spread across the energy and thickness region under investigation. The color shows the ratio between calculation and simulation. In order to only display data with a low statistical uncertainty, simulation values below 1e−5 are not included in the analysis. The calculated iso-line for 1e−5 transmission is presented in black in the left plot, which is seen to closely follow where the simulation data drops below 1e−5

Figure 16 Aluminum, a two-dimensional comparison between calculation and simulation. The transmission and albedo comparisons are shown in the left and right plot, respectively. The comparison is done for all combinations of 20 energies and 20 thicknesses evenly spread across the energy and thickness region under investigation. The color shows the ratio between calculation and simulation. In order to only display data with a low statistical uncertainty, simulation values below 1e−5 are not included in the analysis. The calculated iso-line for 1e−5 albedo is presented in black in the right plot, which is seen to closely follow where the simulation data drops below 1e−5

shielding thickness (*y*-axis). The transmission and albedo is compared separately in the left and right subplots, respectively. The colors correspond to the ratio between between the calculation and simulation probabilities for each data point, calculated via the Log_{10} difference between calculation and simulation. In order to retain adequate statistics, simulation values with a probability below 1e−5 are not included in the analysis. The calculated iso-lines for 1e−5 probability is presented in black lines.

Figure 17 Gd$_2$O$_3$, a two-dimensional comparison between calculation and simulation. The transmission and albedo comparisons are shown in the left and right plot, respectively. The comparison is done for all combinations of 20 energies and 20 thicknesses evenly spread across the energy and thickness region under investigation. The color shows the ratio between calculation and simulation. In order to only display data with a low statistical uncertainty, simulation values below 1e−5 are not included in the analysis. The calculated iso-line for 1e−5 transmission is presented in black in the left plot, which is seen to closely follow where the simulation data drops below 1e−5

Figure 18 Epoxy, a two-dimensional comparison between calculation and simulation. The transmission and albedo comparisons are shown in the left and right plot, respectively. The comparison is done for all combinations of 20 energies and 20 thicknesses evenly spread across the energy and thickness region under investigation. The color shows the ratio between calculation and simulation. In order to only display data with a low statistical uncertainty, simulation values below 1e−5 are not included in the analysis

Figures 31 to 43 shows the performance of each material in terms of neutron transmission and albedo, as described in the main text. In the figures, the probability iso-lines for $P_{transmission}$ (blue) and $P_{transmission}^2 \cdot \frac{1}{2}$ (red) are shown as a function energy and thickness for three different probabilities: 1e−2, 1e−3 and 1e−4. Additionally, the albedo saturation thicknesses are shown as a function of energy, together with the corresponding albedo saturation level for each energy. Note that the albedo saturation level is color coded according to the color bar.

Figure 19 Polyethylene, a two-dimensional comparison between calculation and simulation. The transmission and albedo comparisons are shown in the left and right plot, respectively. The comparison is done for all combinations of 20 energies and 20 thicknesses evenly spread across the energy and thickness region under investigation. The color shows the ratio between calculation and simulation. In order to only display data with a low statistical uncertainty, simulation values below 1e−5 are not included in the analysis

Figure 20 $^{nat}B_4C$, a two-dimensional comparison between calculation and simulation. The transmission and albedo comparisons are shown in the left and right plot, respectively. The comparison is done for all combinations of 20 energies and 20 thicknesses evenly spread across the energy and thickness region under investigation. The color shows the ratio between calculation and simulation. In order to only display data with a low statistical uncertainty, simulation values below 1e−5 are not included in the analysis. The calculated iso-line for 1e−5 transmission is presented in black in the left plot, which is seen to closely follow where the simulation data drops below 1e−5

Figure 21 B$_4$C (^{10}B/B: 99 at%), a two-dimensional comparison between calculation and simulation. The transmission and albedo comparisons are shown in the left and right plot, respectively. The comparison is done for all combinations of 20 energies and 20 thicknesses evenly spread across the energy and thickness region under investigation. The color shows the ratio between calculation and simulation. In order to only display data with a low statistical uncertainty, simulation values below 1e−5 are not included in the analysis. The calculated iso-line for 1e−5 transmission is presented in black in the left plot, which is seen to closely follow where the simulation data drops below 1e−5

Figure 22 ^{nat}LiF, a two-dimensional comparison between calculation and simulation. The transmission and albedo comparisons are shown in the left and right plot, respectively. The comparison is done for all combinations of 20 energies and 20 thicknesses evenly spread across the energy and thickness region under investigation. The color shows the ratio between calculation and simulation. In order to only display data with a low statistical uncertainty, simulation values below 1e−5 are not included in the analysis. The calculated iso-lines for 1e−5 probability is presented in black for transmission and albedo in the left and right plot, respectively

Figure 23 LiF (^{6}Li/Li: 99 at%), a two-dimensional comparison between calculation and simulation. The transmission and albedo comparisons are shown in the left and right plot, respectively. The comparison is done for all combinations of 20 energies and 20 thicknesses evenly spread across the energy and thickness region under investigation. The color shows the ratio between calculation and simulation. In order to only display data with a low statistical uncertainty, simulation values below 1e−5 are not included in the analysis. The calculated iso-lines for 1e−5 probability is presented in black for transmission and albedo in the left and right plot, respectively

Figure 24 MirroBor, a two-dimensional comparison between calculation and simulation. The transmission and albedo comparisons are shown in the left and right plot, respectively. The comparison is done for all combinations of 20 energies and 20 thicknesses evenly spread across the energy and thickness region under investigation. The color shows the ratio between calculation and simulation. In order to only display data with a low statistical uncertainty, simulation values below 1e−5 are not included in the analysis. The calculated iso-line for 1e−5 transmission is presented in the left plot in black

Figure 25 Epoxy-$^{nat}B_4C$ (50 wt% epoxy + 50 wt% $^{nat}B_4C$), a two-dimensional comparison between calculation and simulation. The transmission and albedo comparisons are shown in the left and right plot, respectively. The comparison is done for all combinations of 20 energies and 20 thicknesses evenly spread across the energy and thickness region under investigation. The color shows the ratio between calculation and simulation. In order to only display data with a low statistical uncertainty, simulation values below 1e−5 are not included in the analysis. The calculated iso-line for 1e−5 transmission is presented in black in the left plot

Figure 26 Epoxy-B_4C, $^{10}B/B$: 99 at% (50 wt% epoxy + 50 wt% B_4C), a two-dimensional comparison between calculation and simulation. The transmission and albedo comparisons are shown in the left and right plot, respectively. The comparison is done for all combinations of 20 energies and 20 thicknesses evenly spread across the energy and thickness region under investigation. The color shows the ratio between calculation and simulation. In order to only display data with a low statistical uncertainty, simulation values below 1e−5 are not included in the analysis. The calculated iso-line for 1e−5 transmission is presented in black in the left plot

Figure 27 Epoxy-Gd$_2$O$_3$ (50 wt% epoxy + 50 wt% Gd$_2$O$_3$), a two-dimensional comparison between calculation and simulation. The transmission and albedo comparisons are shown in the left and right plot, respectively. The comparison is done for all combinations of 20 energies and 20 thicknesses evenly spread across the energy and thickness region under investigation. The color shows the ratio between calculation and simulation. In order to only display data with a low statistical uncertainty, simulation values below 1e–5 are not included in the analysis. The calculated iso-line for 1e–5 transmission is presented in black in the left plot

Figure 28 Epoxy-Gd$_2$O$_3$ (35 wt% epoxy + 65 wt% Gd$_2$O$_3$), a two-dimensional comparison between calculation and simulation. The transmission and albedo comparisons are shown in the left and right plot, respectively. The comparison is done for all combinations of 20 energies and 20 thicknesses evenly spread across the energy and thickness region under investigation. The color shows the ratio between calculation and simulation. In order to only display data with a low statistical uncertainty, simulation values below 1e–5 are not included in the analysis. The calculated iso-line for 1e–5 transmission is presented in black in the left plot

Figure 29 Boral (90 wt% Al + 10 wt% $^{nat}B_4C$), a two-dimensional comparison between calculation and simulation. The transmission and albedo comparisons are shown in the left and right plot, respectively. The comparison is done for all combinations of 20 energies and 20 thicknesses evenly spread across the energy and thickness region under investigation. The color shows the ratio between calculation and simulation. In order to only display data with a low statistical uncertainty, simulation values below 1e−5 are not included in the analysis. The calculated iso-lines for 1e−5 probability is presented in black for transmission and albedo in the left and right plot, respectively

Figure 30 Boral (33 wt% Al + 67 wt% $^{nat}B_4C$), a two-dimensional comparison between calculation and simulation. The transmission and albedo comparisons are shown in the left and right plot, respectively. The comparison is done for all combinations of 20 energies and 20 thicknesses evenly spread across the energy and thickness region under investigation. The color shows the ratio between calculation and simulation. In order to only display data with a low statistical uncertainty, simulation values below 1e−5 are not included in the analysis. The calculated iso-lines for 1e−5 probability is presented in black for transmission in the left plot

Figure 31 Cadmium, material properties needed for shielding investigation. The probability iso-lines for $P_{transmission}$ (blue) and $P_{transmission}^2 \cdot \frac{1}{2}$ (red) are shown as a function thickness and energy for three different probabilities: 1e–2, 1e–3 and 1e–4. Additionally, the albedo saturation thicknesses are shown as a function of energy, where the color indicates the albedo saturation level

Figure 32 $^{nat}Gd_2O_3$, material properties needed for shielding investigation The probability iso-lines for $P_{transmission}$ (blue) and $P^2_{transmission} \cdot \frac{1}{2}$ (red) are shown as a function of thickness and energy for three different probabilities: 1e–2, 1e–3 and 1e–4. Additionally, the albedo saturation thicknesses are shown as a function of energy, where the color indicates the albedo saturation level
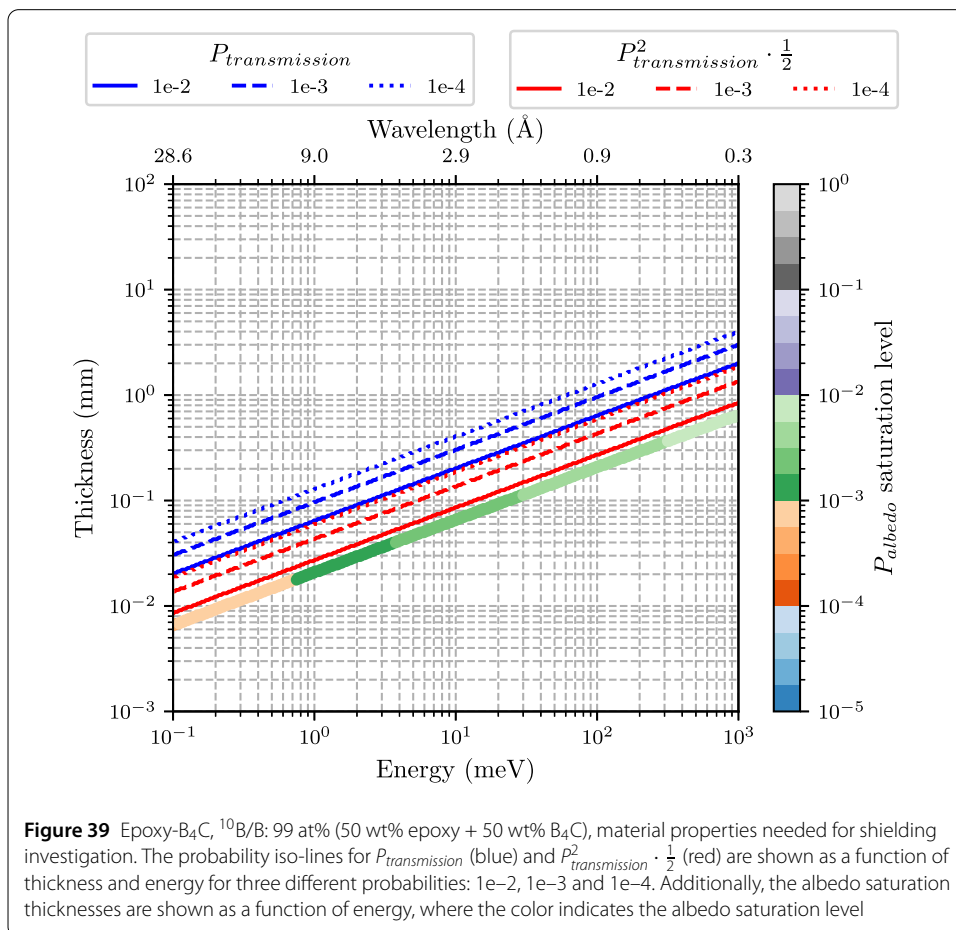
Figure 33 $^{nat}B_4C$, material properties needed for shielding investigation. The probability iso-lines for $P_{transmission}$ (blue) and $P_{transmission}^2 \cdot \frac{1}{2}$ (red) are shown as a function of thickness and energy for three different probabilities: 1e–2, 1e–3 and 1e–4. Additionally, the albedo saturation thicknesses are shown as a function of energy, where the color indicates the albedo saturation level
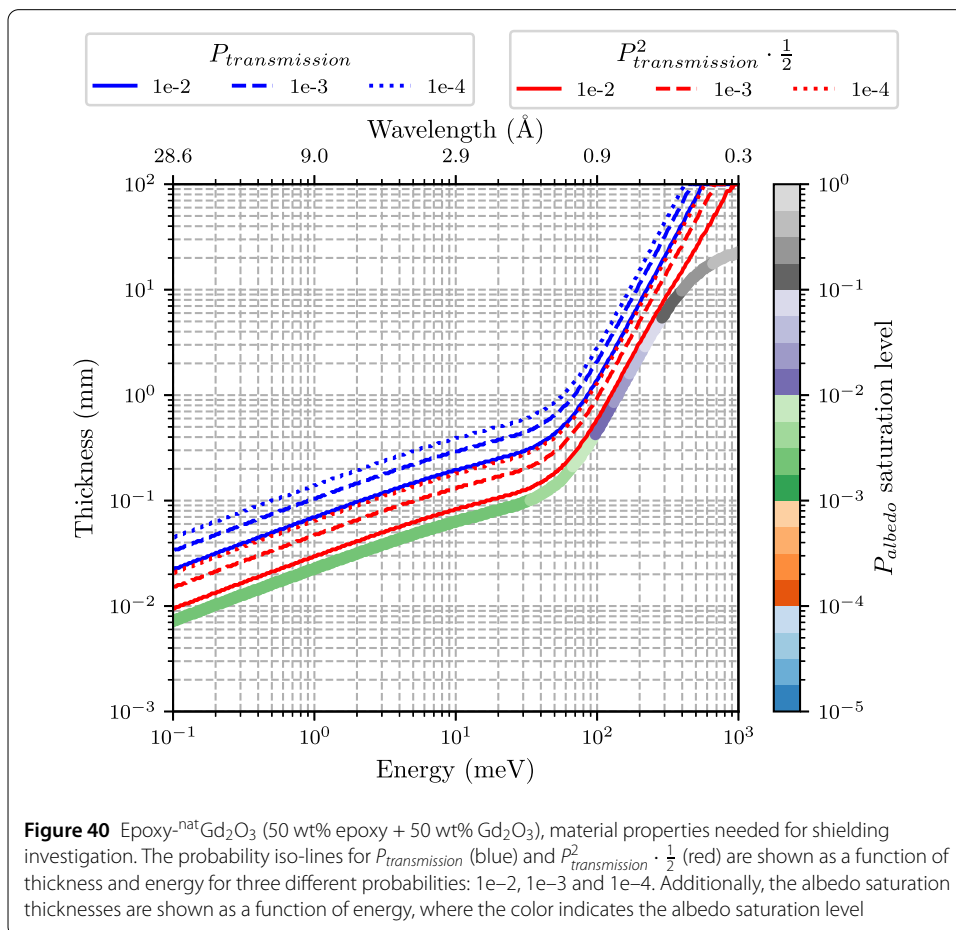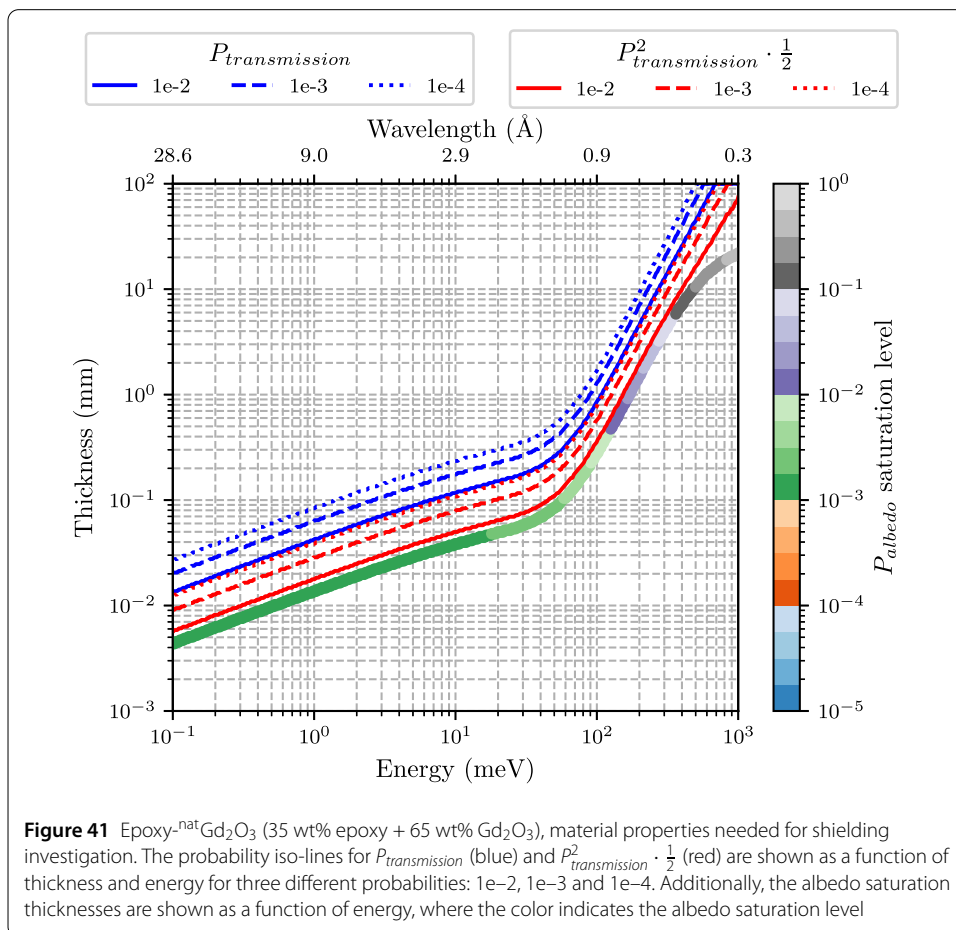
Figure 34 B_4C (^{10}B/B: 99 at%), material properties needed for shielding investigation. The probability iso-lines for $P_{transmission}$ (blue) and $P^2_{transmission} \cdot \frac{1}{2}$ (red) are shown as a function of thickness and energy for three different probabilities: 1e–2, 1e–3 and 1e–4. Additionally, the albedo saturation thicknesses are shown as a function of energy, where the color indicates the albedo saturation level

Figure 35 ^{nat}LiF, material properties needed for shielding investigation. The probability iso-lines for $P_{transmission}$ (blue) and $P^2_{transmission} \cdot \frac{1}{2}$ (red) are shown as a function of thickness and energy for three different probabilities: 1e–2, 1e–3 and 1e–4. Additionally, the albedo saturation thicknesses are shown as a function of energy, where the color indicates the albedo saturation level
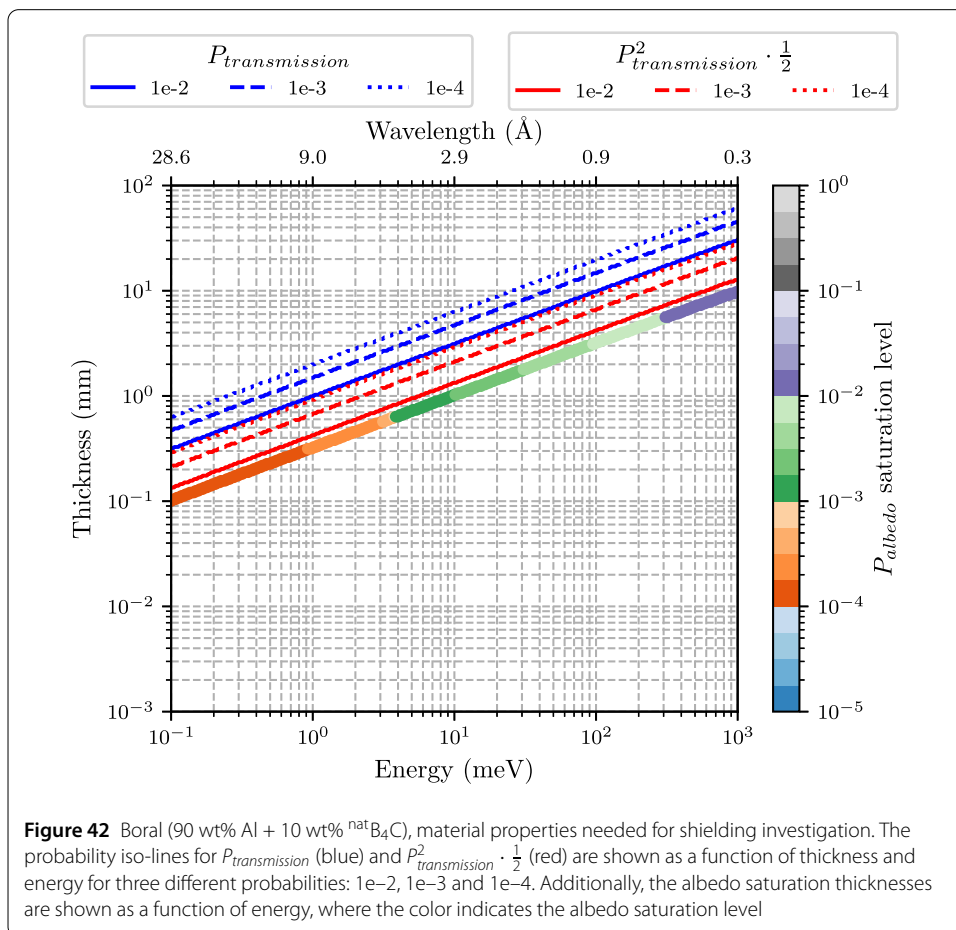
Figure 36 LiF (^{6}Li/Li: 99 at%), material properties needed for shielding investigation. The probability iso-lines for $P_{transmission}$ (blue) and $P_{transmission}^2 \cdot \frac{1}{2}$ (red) are shown as a function of thickness and energy for three different probabilities: 1e–2, 1e–3 and 1e–4. Additionally, the albedo saturation thicknesses are shown as a function of energy, where the color indicates the albedo saturation level

Figure 37 MirroBor, material properties needed for shielding investigation. The probability iso-lines for $P_{transmission}$ (blue) and $P_{transmission}^2 \cdot \frac{1}{2}$ (red) are shown as a function of thickness and energy for three different probabilities: 1e–2, 1e–3 and 1e–4. Additionally, the albedo saturation thicknesses are shown as a function of energy, where the color indicates the albedo saturation level
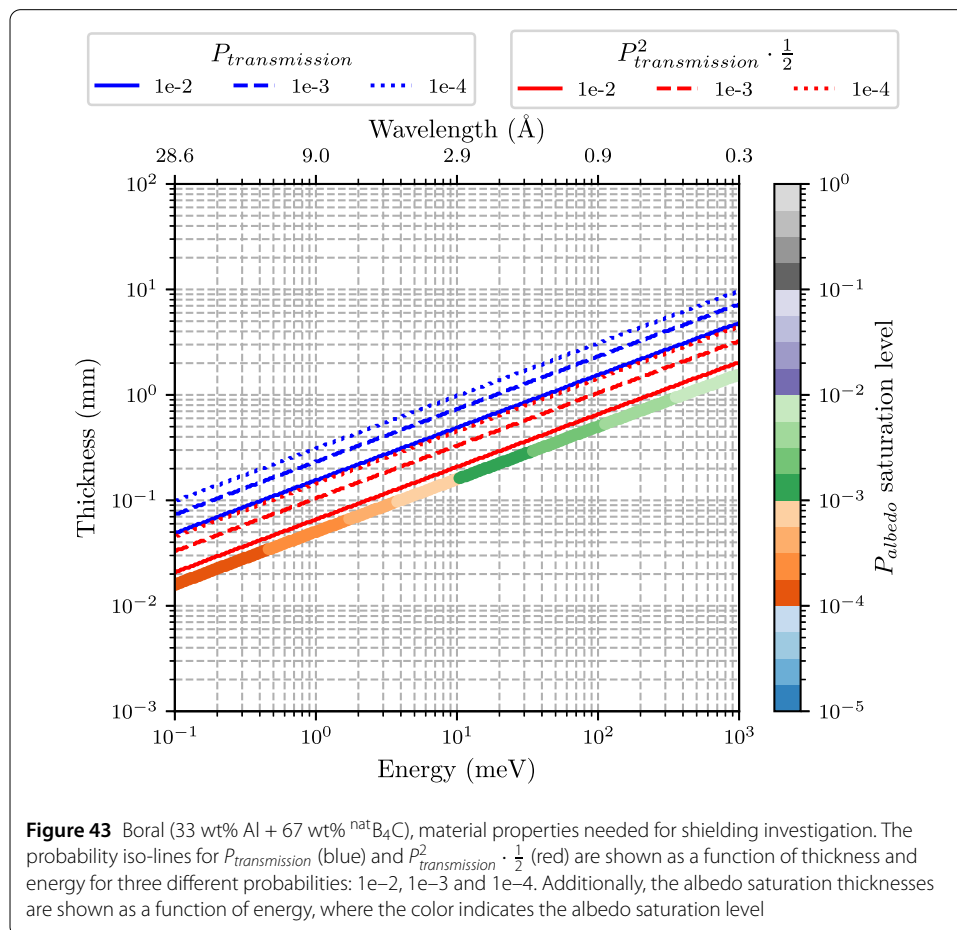
Figure 38 Epoxy-$^{nat}B_4C$ (50 wt% epoxy + 50 wt% $^{nat}B_4C$), material properties needed for shielding investigation. The probability iso-lines for $P_{transmission}$ (blue) and $P_{transmission}^2 \cdot \frac{1}{2}$ (red) are shown as a function of thickness and energy for three different probabilities: 1e–2, 1e–3 and 1e–4. Additionally, the albedo saturation thicknesses are shown as a function of energy, where the color indicates the albedo saturation level

Figure 39 Epoxy-B$_4$C, ^{10}B/B: 99 at% (50 wt% epoxy + 50 wt% B$_4$C), material properties needed for shielding investigation. The probability iso-lines for $P_{transmission}$ (blue) and $P_{transmission}^2 \cdot \frac{1}{2}$ (red) are shown as a function of thickness and energy for three different probabilities: 1e–2, 1e–3 and 1e–4. Additionally, the albedo saturation thicknesses are shown as a function of energy, where the color indicates the albedo saturation level

Figure 40 Epoxy-^{nat}Gd$_2$O$_3$ (50 wt% epoxy + 50 wt% Gd$_2$O$_3$), material properties needed for shielding investigation. The probability iso-lines for $P_{transmission}$ (blue) and $P^2_{transmission} \cdot \frac{1}{2}$ (red) are shown as a function of thickness and energy for three different probabilities: 1e–2, 1e–3 and 1e–4. Additionally, the albedo saturation thicknesses are shown as a function of energy, where the color indicates the albedo saturation level

Figure 41 Epoxy-^{nat}Gd$_2$O$_3$ (35 wt% epoxy + 65 wt% Gd$_2$O$_3$), material properties needed for shielding investigation. The probability iso-lines for $P_{transmission}$ (blue) and $P^2_{transmission} \cdot \frac{1}{2}$ (red) are shown as a function of thickness and energy for three different probabilities: 1e–2, 1e–3 and 1e–4. Additionally, the albedo saturation thicknesses are shown as a function of energy, where the color indicates the albedo saturation level

Figure 42 Boral (90 wt% Al + 10 wt% ^{nat}B$_4$C), material properties needed for shielding investigation. The probability iso-lines for $P_{transmission}$ (blue) and $P^2_{transmission} \cdot \frac{1}{2}$ (red) are shown as a function of thickness and energy for three different probabilities: 1e−2, 1e−3 and 1e−4. Additionally, the albedo saturation thicknesses are shown as a function of energy, where the color indicates the albedo saturation level

Figure 43 Boral (33 wt% Al + 67 wt% ^{nat}B$_4$C), material properties needed for shielding investigation. The probability iso-lines for $P_{transmission}$ (blue) and $P^2_{transmission} \cdot \frac{1}{2}$ (red) are shown as a function of thickness and energy for three different probabilities: 1e−2, 1e−3 and 1e−4. Additionally, the albedo saturation thicknesses are shown as a function of energy, where the color indicates the albedo saturation level

Abbreviations
ESS, European Spallation Source; ILL, Institut Laue–Langevin; MWPC, Multi-Wire Proportional Counter; DG, Detector Group; wt%, Weight percentage; at%, Atomic percentage; SBR, Signal-to-Background Ratio.

Availability of data and materials
The datasets generated and analysed during the current study are available in the *General considerations for effective thermal neutron shielding in detector applications - Analysis & Data* repository, https://doi.org/10.5281/zenodo.6117346. This repository can also be found on GitHub, https://github.com/ess-dg/neutron_shielding_calculations/releases/tag/v1.0.0, and contains all of the code used for the analytical calculations. Instructions on how to run the code and interpret the data is included in the 'README.md'-file in the project. The code used for the simulations during the current study are available from the corresponding author on reasonable request. The ambition is to also make the simulation code publicly available in the near future.

Declarations

Competing interests
The authors declare that they have no competing interests.

Author contributions
AB drafted the manuscript, with the aid of the rest of the authors, and performed the data analysis. TK is one of the main developers of the NCrystal package and implemented the epoxy mixture in NCrystal. AB and RHW conceived the conceptual model developed in this manuscript. All authors contributed with the development of the shielding evaluation framework and how the presentation of results should be structured. Furthermore, all authors participated in the interpretation of results and gave input on how the analysis should be performed. All authors read and approved the final manuscript.

Author details
[1] School of Physics & Astronomy, University of Glasgow, Glasgow, UK. [2] European Spallation Source ERIC, Lund, Sweden. [3] Division of Nuclear Physics, Lund University, Lund, Sweden. [4] Department of Physics, Università degli Studi di Milano-Bicocca, Milano, Italy. [5] Sensors and Devices Centre, Fondazione Bruno Kessler, via Sommarive 18, 38123 Trento, Italy.

Publisher's Note
Springer Nature remains neutral with regard to jurisdictional claims in published maps and institutional affiliations.

References
1. Cherkashyna N et al. High energy particle background at neutron spallation sources and possible solutions. J Phys Conf Ser. 2014;528:012013. https://doi.org/10.1088/1742-6596/528/1/012013.
2. Cherkashyna N et al. Overcoming high energy backgrounds at pulsed spallation sources. In: Proceedings of the 21st meeting of the international collaboration on advanced neutron sources ICANS-XXI JAEA-conf 2015-002 Mito Japan 2014. 2014. https://doi.org/10.11484/jaea-conf-2015-002.
3. Dian E, Kanaki K, Ehlers G, Hall-Wilton RJ, Khaplanov A, Kittelmann T, Zagyvai P. Scattered neutron background in thermal neutron detectors. Nucl Instrum Methods Phys Res, Sect A, Accel Spectrom Detect Assoc Equip. 2018;902:173–83. https://doi.org/10.1016/j.nima.2018.04.055.
4. Dian E, Kanaki K, Khaplanov A, Kittelmann T, Zagyvai P, Hall-Wilton R. Suppression of intrinsic neutron background in the multi-grid detector. J Instrum. 2019;14(01):01021. https://doi.org/10.1088/1748-0221/14/01/p01021.
5. Dian E. Optimisation of signal-to-background ratio for thermal neutron detectors. PhD thesis. Budapest University of Technology and Economics; 2019. https://jinst.sissa.it/jinst/theses/2020_JINST_TH_001.jsp.
6. Guerard B, Buffet JC. Patent EP 2 363 876, Priority Date 2 March 2010.
7. Correa J. 10b4c multi-grid as an alternative to 3he for large area neutron detectors. PhD thesis. University of Zaragoza and Institut Laue-Langevin; 2012. https://zaguan.unizar.es/record/89632#.
8. Khaplanov A, Piscitelli F, Buffet J-C, Clergeau J-F, Correa J, van Esch P, Ferraton M, Guerard B, Hall-Wilton R. Investigation of gamma-ray sensitivity of neutron detectors based on thin converter films. J Instrum. 2013;8(10):10025. https://doi.org/10.1088/1748-0221/8/10/p10025.
9. Khaplanov A et al. Investigation of background in large-area neutron detectors due to alpha emission from impurities in aluminium. J Instrum. 2015;10(10):10019. https://doi.org/10.1088/1748-0221/10/10/p10019.
10. Khaplanov A et al. Multi-grid detector for neutron spectroscopy: results obtained on time-of-flight spectrometer CNCS. J Instrum. 2017;12(04):04030. https://doi.org/10.1088/1748-0221/12/04/p04030.
11. CSPEC. https://europeanspallationsource.se/instruments/cspec. Accessed: 2019-11-29.

12. Deen PP, Longeville S, Lohstroh W, Moreira F, Fabrèges G, Loaiza L, Noferini D. Cspec: the cold chopper spectrometer of the ess, a detailed overview prior to commissioning. Rev Sci Instrum. 2021;92(10):105104. https://doi.org/10.1063/5.0059907.
13. T-REX. https://europeanspallationsource.se/instruments/t-rex. Accessed: 2019-11-29.
14. European Spallation Source. https://europeanspallationsource.se/. Accessed: 2020-01-14.
15. Garoby R et al. The European spallation source design. Phys Scr. 2017;93(1):014001. https://doi.org/10.1088/1402-4896/aa9bff.
16. Peggs S, et al. ESS technical design report [ESS-2013-0001]. Technical report, European Spallation Source. 2013. https://docdb01.esss.lu.se/DocDB/0002/000274/006/TDR_final_130423_print_ch1.pdf.
17. Andersen KH et al. The instrument suite of the European spallation source. Nucl Instrum Methods Phys Res, Sect A, Accel Spectrom Detect Assoc Equip. 2020;957:163402. https://doi.org/10.1016/j.nima.2020.163402.
18. Agostinelli S et al. Geant4—a simulation toolkit. Nucl Instrum Methods Phys Res, Sect A, Accel Spectrom Detect Assoc Equip 2003;506(3):250–303. https://doi.org/10.1016/S0168-9002(03)01368-8.
19. Allison J et al. Recent developments in geant4. Nucl Instrum Methods Phys Res, Sect A, Accel Spectrom Detect Assoc Equip. 2016;835:186–225. https://doi.org/10.1016/j.nima.2016.06.125.
20. Allison J et al. Geant4 developments and applications. IEEE Trans Nucl Sci. 2006;53(1):270–8. https://doi.org/10.1109/TNS.2006.869826.
21. Stone MB, Crow L, Fanelli VR, Niedziela JL. Characterization of shielding materials used in neutron scattering instrumentation. Nucl Instrum Methods Phys Res, Sect A, Accel Spectrom Detect Assoc Equip. 2019;946:162708. https://doi.org/10.1016/j.nima.2019.162708.
22. Kittelmann T et al. Geant4 based simulations for novel neutron detector development. J Phys Conf Ser. 2014;513:022017. https://doi.org/10.1088/1742-6596/513/2/022017.
23. Kanaki K et al. Simulation tools for detector and instrument design. Physica B, Condens Matter. 2018;551:386–9. https://doi.org/10.1016/j.physb.2018.03.025.
24. Piscitelli F. Boron-10 layers, neutron reflectometry and thermal neutron gaseous detectors. PhD thesis. Institut Laue-Langevin and University of Perugia; 2014. https://jinst.sissa.it/jinst/theses/2021_JINST_TH_001.jsp.
25. Cai X-X, Kittelmann T. Ncrystal: a library for thermal neutron transport. Comput Phys Commun. 2020;246:106851. https://doi.org/10.1016/j.cpc.2019.07.015.
26. Kittelmann T, Cai X-X. Elastic neutron scattering models for ncrystal. Comput Phys Commun. 2021;267:108082. https://doi.org/10.1016/j.cpc.2021.108082.
27. Cai X-X, Kittelmann T, Klinkby E, Márquez Damián Jl. Rejection-based sampling of inelastic neutron scattering. J Comput Phys. 2019;380:400–7. https://doi.org/10.1016/j.jcp.2018.11.043.
28. Mirrortron Radiation Shielding. https://mirrotron.com/en/products/radiation-shielding. Accessed: 2021-12-10.
29. 3M™ Advanced Metal Matrix Composite. https://www.3m.com/3M/en_US/p/d/b5005056390/. Accessed: 2022-02-14.
30. Araldite 506 epoxy resin. https://www.chemsrc.com/en/cas/25068-38-6_683612.html. Accessed: 2020-12-8.
31. DiJulio DD, Björgvinsdóttir H, Zendler C, Bentley PM. Population-based metaheuristic optimization in neutron optics and shielding design. Nucl Instrum Methods Phys Res, Sect A, Accel Spectrom Detect Assoc Equip. 2016;835:157–62. https://doi.org/10.1016/j.nima.2016.08.035.
32. Sullivan AH. A guide to radiation and radioactivity levels near high energy particle accelerators. Ashford: Nuclear Technology Publishing; 1992. ISBN: 1 870965 18 3.
33. Stevenson GR, Thomas RH. A simple procedure for the estimation of neutron skyshine from proton accelerators. Health Phys. 1984;46:115–22. https://doi.org/10.1097/00004032-198401000-00009.
34. DiJulio DD, Cooper-Jensen CP, Perrey H, Fissum K, Rofors E, Scherzinger J, Bentley PM. A polyethylene-b_4c based concrete for enhanced neutron shielding at neutron research facilities. Nucl Instrum Methods Phys Res, Sect A. 2017;859:41–6. https://doi.org/10.1016/j.nima.2017.03.064.
35. Bentley PM, Hall-Wilton R, Cooper-Jensen CP, Cherkashyna N, Kanaki K, Schanzer C, Schneider M, Böni P. Self-shielding copper substrate neutron supermirror guides. J Phys Commun. 2021;5:055009. https://doi.org/10.1088/2399-6528/abfae3.
36. Cherkashyna N et al. High energy particle background at neutron spallation sources and possible solutions. J Phys Conf Ser. 2014;528:012013. https://doi.org/10.1088/1742-6596/528/1/012013.
37. Bentley PM. Fast neutron backgrounds: an analysis of likely early operational challenges for the european spallation source. 2022. ESS internal technical report [ESS-4123286].